11

Experimental and Computational Investigation of Nonaqueous Mg/O_2 Batteries

Jeffrey G. Smith[1*], *Gülin Vardar*[2*], *Charles W. Monroe*[3], *and Donald J. Siegel*[1,2,4,5]

[1] *University of Michigan, Department of Mechanical Engineering, Ann Arbor, MI 48109-2125, USA*
[2] *University of Michigan, Department of Materials Science and Engineering, Ann Arbor, MI 48109-2125, USA*
[3] *University of Oxford, Department of Engineering Science, Parks Road, Oxford OX1 3PJ, UK*
[4] *University of Michigan, Applied Physics Program, Ann Arbor, MI 48109-2125, USA*
[5] *University of Michigan, Energy Institute, Ann Arbor, MI 48109-2125, USA*

11.1 Introduction

Highly energetic spontaneous electrochemical reactions occur between metals and oxygen. *Metal/O_2* batteries based on alkali or alkaline earth metals are among the few systems whose theoretical energy densities can compete with automotive propulsion systems based on combustion [1, 2]. To achieve their theoretically promised capacity, metal/O_2 chemistries must incorporate electrolytes that function reversibly without degradation at high voltage and include oxygen electrodes that have low overpotentials for both oxygen reduction and oxygen evolution. More than two decades ago, Abraham and Jiang's work demonstrated that it was possible to produce a reversible high-voltage Li/O_2 cell by using an aprotic solvent and a porous carbon gas-breathing electrode [3]. This pioneering work demonstrated that high-voltage discharge was practically achievable, sparking widespread research into electrolytes, solvents, and other components for Li/O_2 battery systems.

More recently, the secondary metal/O_2 battery community has broadened its focus to explore active metals besides Li, including Na [4] and K [5]. These systems circumvent some of the challenges Li/O_2 systems pose by employing abundant metals that have greater morphological stability during charge/discharge. Higher-alkali/O_2 systems also tend to be more electrochemically reversible and operate with smaller overpotential than Li/O_2. These benefits come at the expense of energy density, however, because Na and K are heavier than Li and each reacts with O_2 at a voltage lower than Li. Chen and Amine concisely summarized the theoretical energy densities provided by a variety of metal/O_2 chemistries in comparison to present-day Li-ion cells [6]. Their report demonstrates that multivalent metals could in principle produce

*These authors contributed equally to this chapter.

Metal–Air Batteries: Fundamentals and Applications, First Edition. Edited by Xin-bo Zhang.

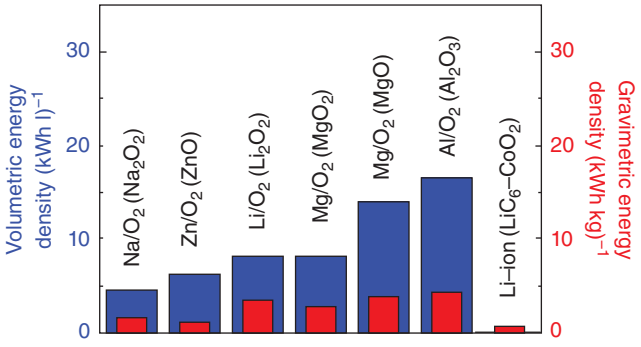

Figure 11.1 Theoretical volumetric and gravimetric energy densities for metal/O_2 and Li ion battery chemistries. For metal/O_2 chemistries, the compound in parenthesis indicates the assumed discharge product. *Source:* Zu and Li 2011 [7]. Reproduced with permission of the Royal Society of Chemistry.

very competitive air batteries. Figure 11.1 provides a graphical comparison of the theoretical and gravimetric energy densities of a variety of metal/oxygen chemistries.

Metal/air batteries consist of a metal negative electrode (an anode during discharge) and a gas-breathing positive electrode (cathode) with either an aqueous or a nonaqueous electrolyte [8]. Examples of metal/air chemistries where the reactant (O_2) is harvested from air include the zinc/air and aluminum/air systems [9, 10]. However, metal/air batteries that use air as the O_2 source are generally not electrochemically reversible due to the presence of water vapor, carbon dioxide, or nitrogen, which lead to parasitic reactions that consume cycleable metal. Replacement of the degraded metal anode with a fresh metal anode is the only option for extended battery use (in combination with a scheme to regenerate spent anodes with an external thermochemical process; this could be called *mechanical recharging*) [11, 12]. Alternatively, the electrolyte in contact with the anode could be water based (as in the aqueous Mg/air battery), but this option sacrifices the power and energy advantages provided by high-voltage electrochemistry [13–15].

Among the multivalent options, Mg/O_2 batteries offer some of the highest theoretical volumetric and gravimetric energy densities. For example, the gravimetric energy density for a Mg/O_2 battery that discharges to MgO, 3.9 kWh kg^{-1}, can theoretically outperform that of a Li/O_2 battery that discharges to Li_2O_2, 3.4 kWh kg^{-1}. Mg also may be safer, cheaper, and less environmentally damaging over the long term. Catastrophic failures of Li-ion batteries often owe to Li dendrite formation, but Mg electrodes have been found to be more resistant to dendrites [16]. As of June 2017, the cost for Mg metal was \$2.32 kg^{-1}, whereas metallic Li costs \$200 kg^{-1} [17]; these prices reflect the far greater natural abundance of Mg. The prevalence of Mg as a structural material has also resulted in the creation of mature recycling technologies.

Primary air-battery chemistries based on Zn and Al were commercialized as far back as the 1990s [18]. To develop a rechargeable Mg/O_2 cell, however, requires substantial material advances. It is critical to produce chemical environments

that foster reversible cell reactions – both at the Mg anode surface and at the air electrode. It is also important to pursue electrolytes that facilitate the motion of ions containing Mg but do not degrade with electrochemical cycling or in the presence of contaminants. This chapter provides a survey of recent experimental and theoretical work that has been performed to address the challenges associated with secondary Mg/O_2 batteries.

Section 11.2 presents a number of experimental studies. These primarily focus on the development and assessment of liquid electrolytes that support the reversible plating and stripping of Mg metal while also providing electrochemical stability at the high potentials associated with oxygen reduction and evolution. Various chemical strategies help to tune electrolyte properties, and these appear to affect both anode functionality and the structure of the discharge product formed in the cell. Electrochemical impedance spectroscopy (EIS) works in combination with several micrographic and spectroscopic methods to illustrate the properties of the discharge product films and other interfaces formed in working Mg/O_2 cells.

Section 11.3 focuses on computational methods that can be applied to study reaction pathways and transport limitations in the expected discharge products of Mg/O_2 cells. These studies identify challenges that need to be overcome to enable efficient, reversible cycling.

11.2 Experimental Studies of Magnesium/Air Batteries and Electrolytes

One barrier impeding the commercialization of Mg-based batteries (both for Mg–ion and Mg/O_2 systems) is the lack of stable and efficient Mg electrolytes. In this section we review several classes of Mg electrolytes (ionic liquids (ILs), modified Grignard systems, and all-inorganic electrolytes) in the context of Mg/O_2 applications. We begin our discussion with electrolytes based on ILs.

11.2.1 Ionic Liquids as Candidate Electrolytes for Mg/O_2 Batteries

ILs are ideal candidates for electrolytes in battery applications due to their low flammability and volatility [19–22]. ILs are ionic compounds that are liquid at room temperature and therefore have high ionic conductivity ($\sim$10 mS cm^{-1}) [21]. They also exhibit high thermal stability and wide electrochemical windows [23]. The drawbacks for ILs are their relatively high viscosity [21] and higher cost compared with organic solvents [24].

ILs have been studied for Li-ion applications [25, 26], and Li metal can be reversibly deposited with high coulombic efficiency using lithium bis (trifluoromethanesulfonyl)imide ($Li(Tf_2N)$) in *N*-methyl-*N*-propylpiperidinium (PP13)-Tf_2N [27]. High-energy-density systems such as Li/O_2 and Li/S have also been explored with IL electrolytes [28–31]. However, research exploring the use of ILs as solvents for Mg-based electrochemistry has been limited, and some of these reports have been difficult to reproduce.

The first mention of reversible deposition and dissolution of Mg in ILs involved 1 M magnesium trifluoromethanesulfonate ($Mg(TfO)_2$) in

1-*n*-butyl-3-methylimidazolium (BMIM)-BF_4 [32–34]. Later, PP13-Tf_2N with 1 M $Mg(TfO)_2$ was also reported to enable reversible Mg deposition dissolution [35]. Finally, $Mg(TfO)_2$ was dissolved in a mixture of PP13-Tf_2N and BMIM-BF_4, and used to cycle a symmetric Mg/Mg cell for over 200 cycles [36]. Amir et al. subsequently reported that they were unable to reproduce reversible Mg deposition with $Mg(TfO)_2$ in BMIM-BF_4 [37]. Cheek et al. also published a study with several combinations of Mg salts and ILs and reported no reversible Mg deposition at room temperature [38]. Interestingly, it was found that Mg codeposition was possible in a mixture of $Mg(Tf_2N)_2$ and $LiTf_2N$ in *N*,*N*-diethyl-*N*-methyl(2-methoxyethyl)ammonium (DEME)-Tf_2N, but not possible when $LiTf_2N$ was absent [39].

In 1990, Gregory et al. showed that a Mg battery consisting of a Mg metal anode, Grignard-reagent electrolyte, and oxide cathode could be cycled [40]. The low partial charge on Mg in the Grignard molecule was assumed to facilitate desolvation of Mg at the interface where plating occurs. In contrast, electrolytes containing highly ionic compounds such as $MgCl_2$ or $Mg(ClO_4)_2$ did not result in pure Mg metal precipitates at the Mg anode. It was suggested that the highly ionic Mg compounds inhibit Mg deposition due to the inability of Mg^{2+} to dissociate at the anode.

One drawback of the Grignard reagents is their low oxidative stability vs Mg metal. Oxidative stability of these systems ranges from 1.2 to 1.5 V vs $Mg^{2+/0}$, which limits the energy density of a battery using such an electrolyte. Aurbach et al. significantly improved the oxidative stability of Grignard-reagent Mg electrolytes by adding Al-based Lewis acids [41, 42]. Strong Lewis acids enable Mg dissociation due to their strong electron-withdrawing nature, which presumably overcomes the coulomb force that prevents the dissociation of anions from Mg^{2+} (Mg/O_2 batteries using Lewis-acid containing Grignard-reagent Mg electrolytes will be discussed in Section 11.2.2). Recently, solutions of simple Mg salts such as $MgCl_2$ combined with Al-based Lewis acids were shown to reversibly deposit and dissolve Mg [43, 44] (Mg/O_2 batteries using Mg salt electrolytes with Lewis acids will be discussed in Section 11.2.3).

An approach to using ILs as solvents for Mg batteries has been to use Grignard reagents dissolved in tetrahydrofuran (THF) as the Mg source in the electrolyte [45]. Adding DEME-Tf_2N (up to 50 mol%) to solutions of $Mg(HMDS)_2$–$MgCl_2$ in THF increases ionic conductivity due to DEME-Tf_2N being extensively solvated by THF at these concentrations [46]. However, the presence of THF, an organic solvent with high flammability and volatility, still makes these mixed electrolytes susceptible to safety risks. The same can be said for adding ACN and dimethoxyethane (DME) to IL solvents to facilitate Mg deposition [47]. Moreover, Grignard reagents are highly reactive with water. An electrolyte that is free of organic solvents and Grignard reagents would be ideal for safety and stability reasons. Such an electrolyte could use an IL as the solvent and a non-Grignard Mg source, such as a Mg salt.

As previously mentioned, studies of ionic Mg salts dissolved in ILs have been a source of controversy due to reproducibility issues. The nonsystematic choice of anions and cations used in these studies has also impeded the identification of performance trends [37, 38]. To address these concerns, we performed a

systematic study to isolate the effects of IL cation, IL anion, and organic solvent [48].

Cyclic voltammetry was used to investigate the electrochemistry of electrolytic solutions consisting of various Mg salts ($Mg(TfO)_2$, $Mg(Tf_2N)_2$, $Mg(BH_4)_2$), IL solvents (BMIM-Tf_2N, PP13-Tf_2N, DEME-BF_4), and organic cosolvents (DME, ACN) on Pt working electrodes. Contrary to some prior reports, reversible Mg plating was not observed for any of these salt/IL combinations. The disagreement with prior observations of reversible Mg deposition arises, in some cases, from different interpretations of the voltammograms. Robust control experiments such as cyclic voltammograms for the pure IL, cyclic voltammograms in which the identity of the IL cation is varied, and the exploration of wider voltage ranges during voltammetry are necessary. For example, it was found that the anodic peak observed at ~0.8 V vs Mg/Mg^{2+} in the voltammetry of $Mg(TfO)_2$ dissolved in BMIM-BF_4, previously attributed to Mg stripping [32, 33], likely originates from redox activity correlated to the presence of $BMIM^+$ (Figure 11.2).

Computational and experimental studies provide insight for the lack of reversible Mg deposition from salts containing Tf_2N^-. X-ray scattering data show that Mg^{2+} and Tf_2N^- are incompletely dissociated in diglyme [49] (Figure 11.3). The average Mg–O bond distances (2.08 Å) measured in solutions of $Mg(Tf_2N)_2$ in glyme solutions are similar to the Mg–O distances in Mg-based solids such as MgO (2.1–2.6 Å), suggesting that the Mg–Tf_2N interaction is strong [49]. Tf_2N^- anions have also been shown to be more susceptible to bond breaking in the presence of Mg^{2+} compared with other anions such as BH_4^- and BF_4^- [50]. Oxygen reduction reaction (ORR) experiments using $Mg(Tf_{2N})_2$/BMIM-Tf_{2N} showed that the presence of Mg^{2+} induced the degradation of BMIM-TFSA and formation of MgF_2 on the electrode surface, which blocked the electrode for reversible ORR [51].

The strong association of Tf_2N^- and Mg^{2+} could not be overcome by attempts to lower the ion solvation energies by adding high-polarity cosolvents such as ACN and DME. It therefore seems unlikely that simple Mg salts can be used as the Mg source in IL-based electrolytes for secondary Mg batteries unless new

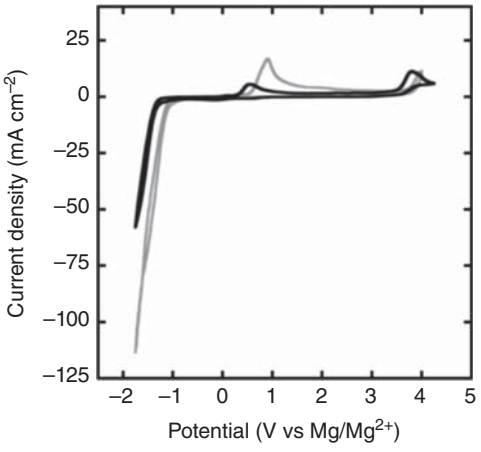

Figure 11.2 Cyclic voltammograms of neat BMIM-Tf_2N (light gray) and 10 mM $Mg(Tf_2N)_2$ in BMIM-Tf_2N (black) on a 50 μm diameter Pt working electrode at room temperature; scan rate 100 mV s^{-1}.

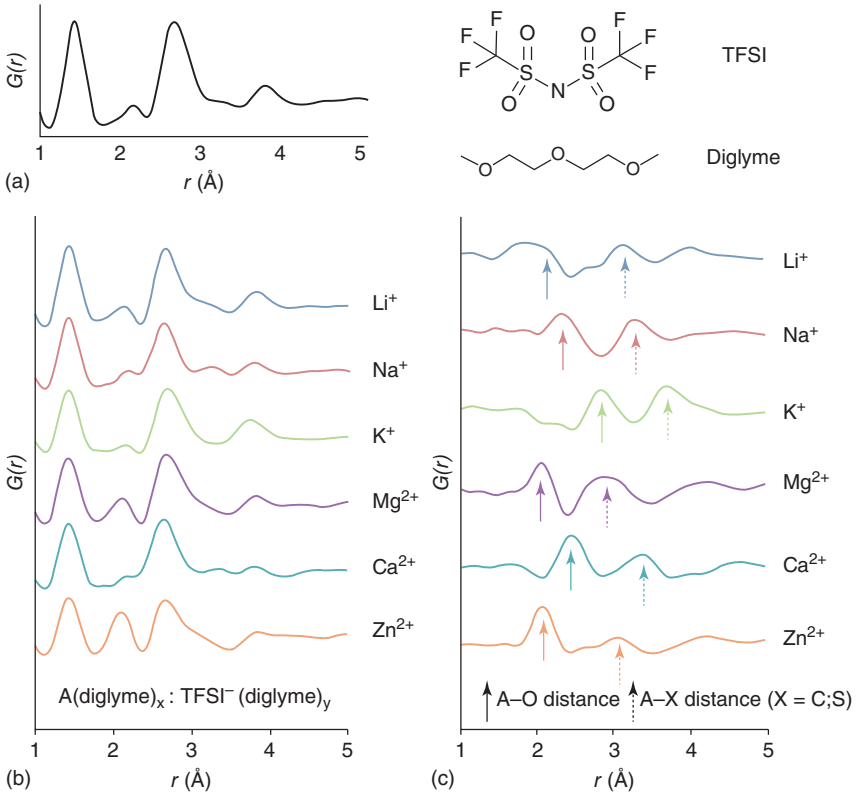

Figure 11.3 Pair distribution function (PDF) for the series of $A(TFSI)_x$–diglyme solutions, A = Li^+, Na^+, K^+, Mg^{2+}, Ca^{2+}, Zn^{2+}, highlighting (a) the common TFSI–TFSI and TFSI–diglyme atom–atom correlations as determined through principal component analysis, (b) the as-measured total PDFs, and (c) the differential PDFs corresponding to the $A^{+/2+}$ solvation environment. Data have been offset for clarity. *Source:* Lapidus et al. 2014 [49]. Reproduced with permission of the Royal Society of Chemistry.

measures are taken to foster dissociation of the Mg salt or lower ion solvation energies significantly. For example, the coordination between Mg^{2+} and Tf_2N^- has been shown to decrease [52] with the addition of MgI_2 and $Mg(ClO_4)_2$ but did not necessarily facilitate reversible Mg deposition from $Mg(Tf_2N)_2$.

$Mg(BH_4)_2$ has been shown to deposit Mg reversibly from organic solvents [53]. Therefore, $Mg(BH_4)_2$ in DEME-BF_4 was also considered in our studies, but no evidence of Mg plating or stripping was observed. Although addition of $Mg(BH_4)_2$ to DEME-BF_4 increased the current response at 1 V vs Mg/Mg^{2+} (compared with DEME-BF_4 alone), this current increase could not be attributed to Mg stripping. A cyclic voltammetry scan with a range of −1 to 1 V vs Mg/Mg^{2+} (Figure 11.4) shows that the net anodic charge transfer above 0 V vs Mg/Mg^{2+} far outweighs the net cathodic charge transfer below 0 V vs Mg/Mg^{2+}, suggesting an oxidation reaction occurring simultaneously with stripping. This example highlights the necessity of exploring sufficiently wide voltage windows to identify the processes associated with the observed current response.

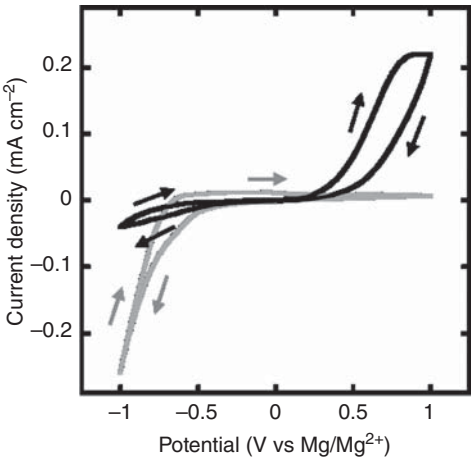

Figure 11.4 Cyclic voltammograms of neat DEME-BF_4 (light gray) and 100 mM $Mg(BH_4)_2$ in DEME-BF_4 (black). Cyclic voltammetry scan limits are constrained to −1 to 1 V vs Mg/Mg^{2+}. Fifty microns diameter Pt-disk working electrode; 100 mV s^{-1} scan rate; room temperature.

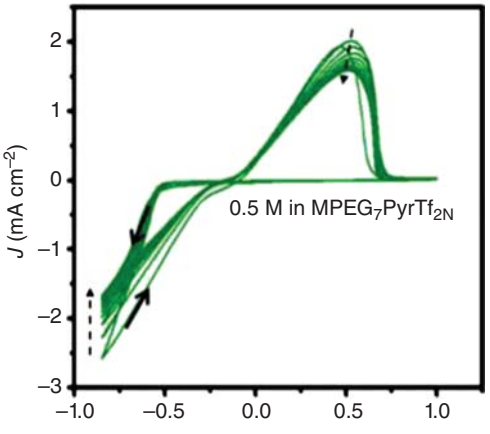

Figure 11.5 Successive cyclic voltammograms for 0.5 M $Mg(BH_4)_2$/$MPEG_7PyrTf_{2N}$ at 25 mV s^{-1}. *Source:* Watkins et al. 2016 [54]. Reproduced with permission of the American Chemical Society.

Research into modifying IL cations has shown that Mg^{2+} and Tf_2N^- coordination can be suppressed by attaching polyether chains to the IL cations [22, 54]. With this approach, it was possible to reversibly deposit Mg using a $Mg(BH_4)_2$ salt dissolved in a Tf_2N-containing IL (Figure 11.5). The main drawback of $Mg(BH_4)_2$ is its low oxidative stability, which is as low as 1 V vs $Mg^{2+/0}$ [53]. However, since the first report on $Mg(BH_4)_2$ as a salt capable of reversible Mg deposition in 2012, oxidative stability has been improved by anion modification [55, 56]. Therefore, it could be possible to have a nonaqueous electrolyte of a Mg salt derived from $Mg(BH_4)_2$ dissolved in a modified IL that could be oxidatively stable in the range of 0–3 V vs $Mg^{2+/0}$ and reversibly deposit Mg. How such an electrolyte would perform in an Mg/O_2 remains to be reported.

11.2.2 Modified Grignard Electrolytes for Mg/O_2 Batteries

As mentioned earlier, a reversible Mg battery using Grignard-reagent electrolytes was reported in the early 1990s [40]. Addition of Al-based Lewis acids to Grignard

reagents has resulted in improved oxidative stability while maintaining highly reversible Mg plating [41]. Therefore, nonaqueous electrolytes such as Grignard reagents dissolved in organic solvents could in theory enable a reversible Mg/O_2 cell with a solid Mg anode. The operation of a Mg/O_2 cell based on a modified Grignard electrolyte is summarized below. Further details can be found in Ref. [57].

In Li/O_2 and Na/O_2 batteries, the reactions expected to take place at the gas electrode, and the resulting discharge products, have been discussed extensively [4, 58–64]. However, there is presently no consensus regarding the discharge mechanisms in Mg/O_2 batteries. In a reversible Mg/O_2 cell, the following reactions may be expected to take place in the O_2 electrode:

$$Mg^{2+} + O_2 + 2e^- \rightleftharpoons MgO_2 \quad \left(2.91 \text{ vs } Mg^{2+/0}\right) \tag{11.1}$$

$$2Mg^{2+} + O_2 + 4e^- \rightleftharpoons 2MgO \quad \left(2.95 \text{ vs } Mg^{2+/0}\right) \tag{11.2}$$

These reactions promise moderately high cell potentials of ~2.9 V if the reaction at the anode is the reversible formation of Mg^{2+} cations from Mg metal. However, the open-circuit potentials observed in Mg/O_2 batteries are well below the expected value of 2.9 V.

Figure 11.6 illustrates the potentials at which the negative and positive electrode reactions are expected to take place for Li/O_2, Na/O_2, K/O_2, and Mg/O_2 batteries. Li/O_2, Na/O_2, and K/O_2 cells exhibit open circuit voltages close to the theoretical values expected from the difference between the positive-electrode half-reaction potential associated with the direct electrochemical formation of the corresponding metal oxide compounds and negative-electrode half-reaction potential associated with formation of metal cations [5, 62, 65]. However, as Figure 11.6 shows, the potential associated with superoxide formation ($O_2 + e^- \rightleftharpoons O_2^-$, – 0.33 V vs SHE (standard hydrogen electrode)) in the alkali

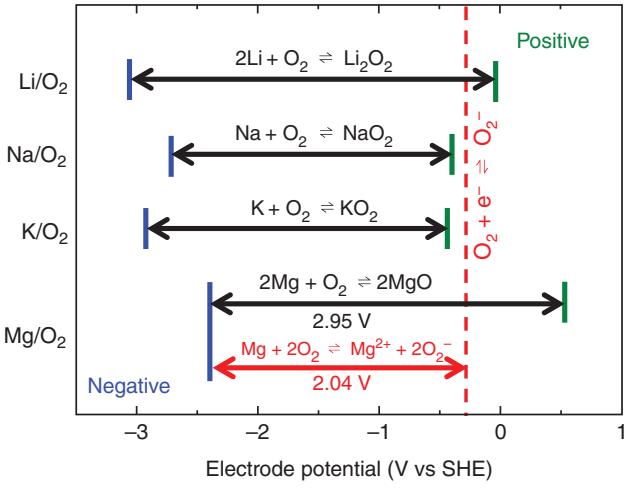

Figure 11.6 Cell potentials and half-reaction potentials for several metal/O_2 battery chemistries. The dashed red line corresponds to the potential at which O_2 reduces to superoxide.

chemistries closely matches the potentials for direct electrochemical M_xO_y formation from Li, Na, and K. In contrast, for Mg/O_2, superoxide forms from O_2 well (~0.9 V) below (2.04 V) the potential for direct electrochemical MgO formation (2.95 V).

In light of the thermodynamic data summarized in Figure 11.6, the lower-than-expected OCV in the Mg/O_2 system suggests a reaction pathway where oxygen reduction (i.e. O_2^- formation) occurs as an initial electrochemical step and is followed by a chemical reaction between the superoxide ion and Mg cations:

$$O_2 + e^- \rightleftharpoons O_2^- \quad (2.04 \text{ V vs } Mg^{2+/0}) \tag{11.3a}$$

$$2O_2^- + Mg^{2+} \rightleftharpoons MgO_2 + O_2 \tag{11.3b}$$

$$2MgO_2 \rightleftharpoons 2MgO + O_2 \tag{11.3c}$$

This hypothesized pathway is an *electrochemical–chemical–chemical* (ECC) mechanism similar to those proposed for Li/O_2 and other alkali metal-based systems [5, 61, 65, 66]. The subsequent chemical steps 11.3b and 11.3c, which MgO_2 and MgO, do not contribute to the electrical work delivered by the cell. Designs that select against the superoxide pathway and support direct electrochemical formation of MgO_x will be needed to realize the promise that the Mg/O_2 chemistry holds for higher energy density.

Figure 11.7 shows discharge/recharge cycles for a typical Mg/O_2 cell using a modified Grignard electrolyte (4 : 1 PhMgCl : $Al(OPh)_3$/THF) that exhibited high (~4 V) oxidative stability vs Mg [67]. The energy efficiency for the first cycle is 42% – low compared with the energy efficiencies reported for nonaqueous Li/O_2, K/O_2, and Na/O_2 chemistries that typically exhibit higher than 80% efficiency, but comparable to those for elevated-temperature Mg/O_2 cells [62, 68–70].

Characterizing the discharge product is an essential step toward identifying the discharge mechanism of Mg/O_2 batteries. The discharge product was characterized using microscopy, diffraction, and spectroscopy. Scanning electron microscopy images showed that the formation of discharge product is limited

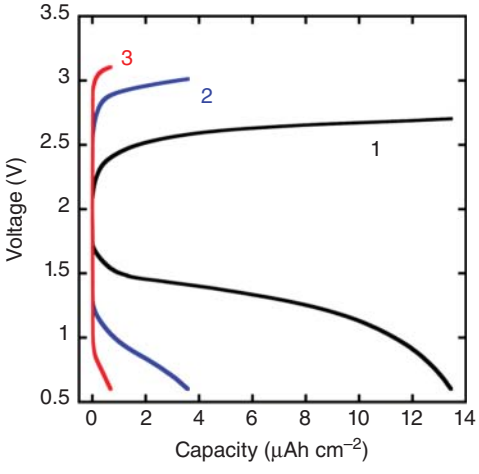

Figure 11.7 Discharge/recharge cycles for a room temperature Mg/O_2 cell using 4 : 1 PhMgCl:$Al(OPh)_3$/THF at 5 μA cm^{-2} (superficial). Curves are labeled with the corresponding cycle numbers.

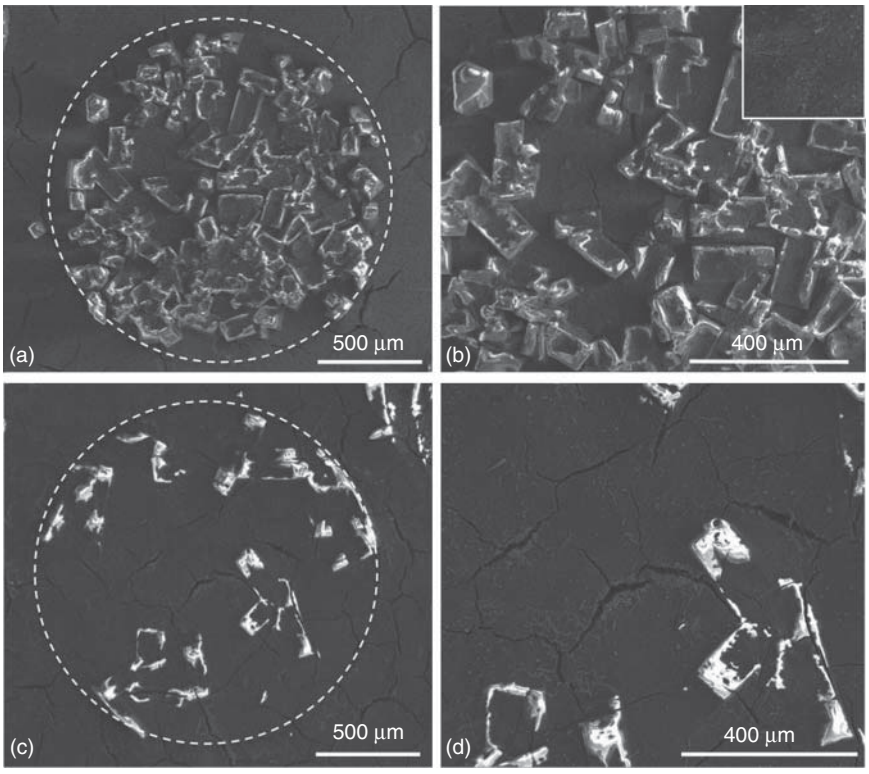

Figure 11.8 SEM images of the positive electrode surface on the side closest to the O_2 gas inlet for Mg/O_2 cell using 4 : 1 PhMgCl:Al(OPh)$_3$/THF electrolyte. The dashed circles represent boundaries of the regions that were directly exposed to O_2 through perforations in the Pt-coated current collector. (a) An electrode after first discharge. (b) Higher magnification of the first-discharge product with an inset image of a control electrode exposed to O_2 in a cell held at open circuit. (c) An electrode at the end of first recharge. (d) Higher magnification of the residual product after first recharge.

to the areas of the cathode with direct exposure to O_2, suggesting that the low permeability of O_2 in the electrolyte could limit the capacity of the battery (Figure 11.8). Spectroscopy and X-ray diffraction measurements on discharged cathodes indicate formation of MgO_2 in addition to MgO. Recharging the battery would ideally result in complete decomposition of the discharge product. However, only partial decomposition was observed in the recharged cathodes. The incomplete disappearance of the discharge product suggests the presence of side reactions, which may explain both the low energy efficiency and the capacity fade upon cycling.

Spectroscopy and diffraction measurements showed that the discharge product remaining after recharge consists entirely of MgO. This suggests that MgO_2 decomposes preferentially during charging. Note that some MgO also must be consumed during the recharge process, because Figure 11.8c shows that more than 30% of the discharge-product volume is consumed.

In summary, a Mg/O_2 cell using a modified Grignard electrolyte produces a mixed-phase product that comprises crystalline MgO with domains of amorphous MgO_2. The discharge reaction is preceded by the electrochemical reduction of O_2^0 to superoxide O_2^-. The chemical precipitation of MgO_2 then is followed by incomplete disproportionation, resulting in some fraction of the discharge product being MgO. The recharged positive electrode contained a small amount of residual MgO, suggesting that MgO_2 decomposes first during charging with more limited MgO decomposition.

The superoxide-controlled discharge voltage, low capacity, and limited cycle life observed for the Mg/O_2 cell presented here suggest that additional development is needed to realize the advantages of Mg/O_2 batteries. Further electrolyte development could increase both capacity and rate performance. In addition, circumventing the multistep discharge mechanism in favor of direct electrochemical MgO_x formation would lead to cells with higher energy density.

11.2.3 All-inorganic Electrolytes for Mg/O_2 Batteries

Prior to the invention of all-inorganic Mg electrolytes in 2012 [43, 53], Grignard-reagent-based electrolytes were thought to be the only class of nonaqueous solutions capable of reversible Mg deposition [40]. However, Grignard solutions exhibit low conductivity ($<1\,mS\,cm^{-1}$) and need to be supported by Lewis acids to achieve oxidative stability above 1 V vs Mg/Mg^{2+} [45, 71, 72]. Also, Grignard reagents are pyrophoric [73], so a Grignard-free electrolyte could have advantages.

Alternatively, simple Mg salts are known to dissociate poorly in organic solvents [53], possibly due to the high charge density on the Mg^{2+}ion [48–50]. Undissociated Mg salts cannot enable reversible Mg deposition and are therefore unsuitable as electrolytes as discussed in Section 11.2.1.

A third electrolyte option is the all-inorganic magnesium aluminum chloride complex (MACC) reported by Doe et al. [43]. MACC is synthesized by reacting a simple Mg salt with a Lewis acid in a nonaqueous solvent such as DME or THF. MACC/DME allows Mg plating and stripping at room temperature with low deposition overpotentials (<300 mV vs $Mg/Mg^{2+/0}$), high coulombic efficiency (>95%), and high oxidative stability (>3 V vs $Mg^{2+/0}$ with a Pt-working electrode). The speciation and conditioning of MACC electrolytes has been studied extensively [74–77].

Parallel to the discovery of MACC in 2014, several other reports explored the complexation of Mg salts to achieve all-inorganic Mg electrolytes [44, 78–81]. The common thread in the development of all-inorganic Mg electrolytes has been the necessity of a Cl-containing species to allow for reversible and efficient Mg deposition. The presence of Cl has been shown to result in corrosion in batteries [82], therefore the presence of Cl is discouraged. However, all-inorganic electrolytes remain of interest due to their facile synthesis and electrochemical simplicity.

A rechargeable, elevated-temperature Mg/O_2 battery using inorganic Mg salts was reported in 2013 [70]. In this case, the electrolyte was $Mg(ClO_4)_2$ dissolved in DMSO, and MgI_2 was added to the solution act as a redox mediator to facilitate

the dissolution of MgO, the predicted discharge product. Although it is unclear whether the electrolyte in this case allows for reversible Mg deposition on the Mg anode, the Mg/O_2 battery showed reasonable cycling and capacity (Figure 11.9). The cycling of the battery was performed at elevated temperatures (60 °C), presumably to facilitate faster kinetics.

Figure 11.10 shows the performance of a Mg/O_2 cell using the MACC electrolyte. This cell exhibits a capacity similar to those of elevated-temperature cells based on simple Mg-salt electrolytes with redox mediators [70, 83]. In addition, the discharge capacity obtained with the MACC/DME electrolyte is much higher than that of the room temperature Mg/O_2 battery based on a modified Grignard electrolyte discussed above.

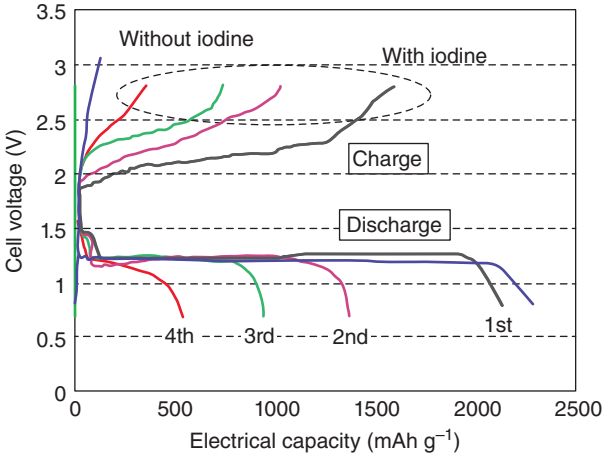

Figure 11.9 Discharge–charge curves of the nonaqueous Mg/O_2 battery with iodine at 60C. The black, pink, green, and red lines correspond to the first, second, third, and fourth cycles, respectively. The blue line represents a discharging–charging profile in the absence of iodine. *Source:* Shiga et al. 2013 [70]. Reproduced with permission of the Royal Society of Chemistry.

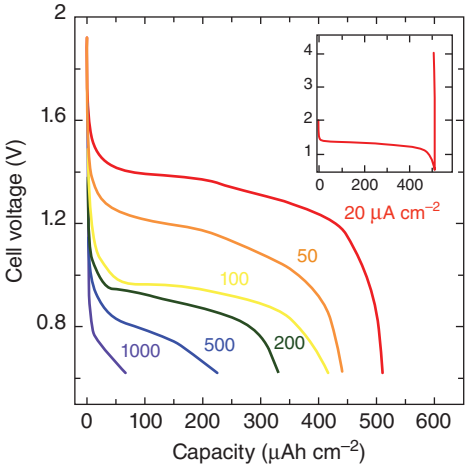

Figure 11.10 Cell voltage vs capacity for a Mg/O_2 cell using the MACC electrolyte discharged at current densities ranging from 0.02 to 1 mA cm^{-2} (superficial). The inset shows a typical discharge/charge cycle at 0.02 mA cm^{-2}.

The large difference in capacities between cells based on Grignard/THF (Figure 11.7) and MACC/DME (Figure 11.10) electrolytes owes at least partially to the higher conductivity of the MACC solution and the higher solubility of O_2 in DME. Indeed, O_2 permeability (defined as the product of saturated O_2 concentration and effective diffusivity) is thought to contribute to capacity limitations in Li/O_2 batteries [64, 84]. The conductivity of the modified Grignard electrolyte was reported to be 1.24 mS cm^{-1} [67], whereas the conductivity of the conditioned MACC/DME was 2.21 mS cm^{-1}. Furthermore, the solubility of O_2 in DME has been reported to be five times higher than in THF [85, 86]. Additional tuning of the electrolyte composition could raise the capacities observed for Mg/O_2 systems. For example, varying the donor number of the solvent appears to have a significant effect on the capacity of nonaqueous Li/O_2 cells [87].

Mg/O_2–MACC/DME cells exhibited negligible recharge capacity at 200 μA cm^{-2} (cf. Figure 11.10 inset). In contrast, Mg/O_2–Grignard/THF cells exhibited nonnegligible recharge capacity, albeit at low recharge rates (5 μA cm^{-2}). The difference in recharge behavior can be attributed to the difference in discharge-product chemistry, as described below.

The discharge product composition for the Mg/O_2–MACC/DME cell was characterized using microscopy, spectroscopy, and diffraction measurements. X-ray diffraction and Raman spectroscopy data show signatures associated with $MgCl_2$ and $Mg(ClO_4)_2$. Spatially resolved characterization techniques indicate that the discharge product is nonuniform. Furthermore, anhydrous $Mg(ClO_4)_2$ can decompose spontaneously into $MgCl_2$ and O_2 at room temperature via the reaction [88]

$$Mg(ClO_4)_2 \rightarrow MgCl_2 + 4O_2. \tag{11.4}$$

Thus, the nonuniform product observed could be explained by electrochemical $Mg(ClO_4)_2$ formation, followed by gradual chemical decomposition into $MgCl_2$ and O_2. The discharge product for Mg/O_2 cells using the MACC/DME electrolyte was found to contain larger amounts of Cl than Mg/O_2 cells using the Grignard electrolyte. The presence of Cl in the discharge product indicates that MACC/DME electrolyte is consumed during or immediately after the electrochemical discharge reaction step [89].

In addition to energy density and rechargeability, rate capability is another important performance metric for batteries. The MACC/DME electrolyte allowed discharge of Mg/O_2 cells at a wide range of current densities, ranging from 0.02 to 1 mA cm^{-2}. These compare favorably to rates at which Li/O_2 cells have been tested, offering the possibility of a direct comparison between Li and Mg chemistries.

Figure 11.11 shows discharge capacity and cell voltage at 50% depth of discharge as functions of the discharge rate from several independently assembled Mg/O_2 cells. The data shows (Figure 11.11a) that discharge rate does not significantly affect capacity at rates below 0.01 mA cm^{-2}. However, capacity decreases dramatically with increasing discharge rate at rates above 0.02 mA cm^{-2}. These characteristic features of the capacity vs rate curve are consistent with the model

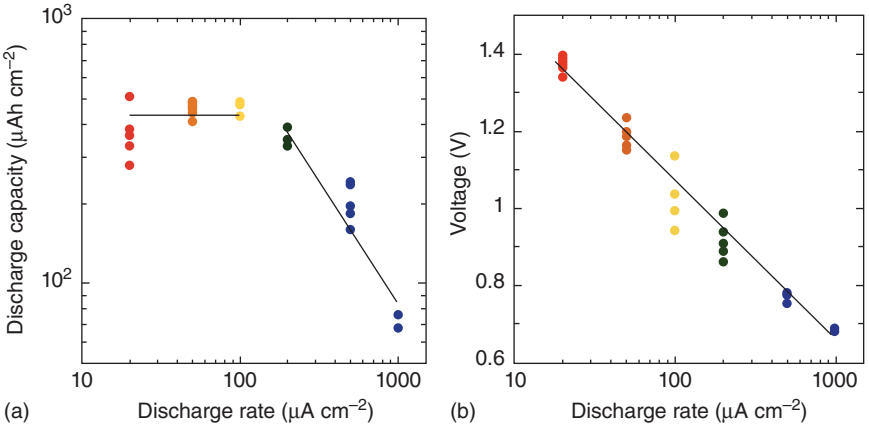

Figure 11.11 (a) Capacity per geometric electrode area achieved at the 0.6 V cutoff potential as a function of discharge rate. Capacity falls as a power law with respect to discharge rate at rates higher than 0.02 mAh cm^{-2}. (b) Cell voltage at 50% depth of discharge as a function of discharge rate.

of Li/O_2 discharge presented by Liu and Monroe, which predicts that the capacity at higher rates falls as a power law with respect to discharge current [84].

The higher-rate data were analyzed using Peukert's law, which is an empirical relation linking discharge capacity, q_{total}, and the discharge current density, i [90]:

$$\ln\left(\frac{q_{\text{total}}}{q_{\text{ref}}}\right) = (1-k)\ \ln\left(\frac{i}{i_{\text{ref}}}\right).$$

here k is the Peukert coefficient, i_{ref} is a reference current density (in this case, 1 mA cm^{-2}), and q_{ref} is the capacity at i_{ref}. The Peukert exponent, k, describes the ability of a battery to retain its capacity with increasing rate and can be compared across different battery chemistries. An ideal battery would have $k = 1$, meaning that the cell capacity is unchanged as a function of discharge rate. (For reference, k values for Li-ion batteries fall within the range of 1.6 ± 0.1 [64], whereas those of Pb/acid cells are nearer 1.4 [91]) Since drawing a current is associated with energy dissipation, $k > 1$. The capacities observed above 0.02 mA cm^{-2} for Mg/O_2 cells using MACC/DME follow a power-law dependence on the discharge current. The calculated Peukert exponent is 1.9, with a reference capacity of 91 μAh cm^{-2} at 1 mA cm^{-2}. This k value agrees well with the assumption that battery performance is limited by liquid-phase O_2 diffusion, which manifests as a Peukert exponent of 2 [84]. Compared to the Li/O_2 chemistry, for which $k = 1.6$ [64], Mg/O_2 cells appear to exhibit lower rate capability. The transition from $k \sim 1$ (below 0.01 mA cm^{-2}) to $k > 1$ (above 0.02 mA cm^{-2}) is commonly observed for metal/O_2 batteries; Liu and Monroe's model suggests that this transition occurs when the discharge current drives product formation sufficiently fast that O_2 is unable to diffuse all the way across the positive electrode [65, 84].

Figure 11.11b shows the cell potential at 50% depth of discharge as a function of discharge rate. Following an analysis similar to that of Viswanathan et al. [92], the present data reveals a Tafel slope of 4.9 V^{-1} and an exchange-current density of

1.6 μA cm^{-2} (superficial). Compared with Li/O_2 cells operated at the same rates (Tafel slope 11 ± 1 V^{-1} and exchange-current density 7 ± 3 μA cm^{-2}), the present Mg/O_2 cells have a lower exchange-current density, suggesting that kinetic overpotentials are higher.

11.2.4 Electrochemical Impedance Spectroscopy

EIS is a useful tool in understanding the interfacial processes that take place in a battery. The evolution of internal resistance in Mg/O_2 batteries can be studied using EIS. Control experiments such as symmetric Mg/Mg cells and exposure to controlled atmospheres are necessary to assign EIS components to interfaces and effects of Ar and O_2.

Figure 11.12a shows Nyquist plots for a symmetric Mg/Mg cell with MACC/DME electrolyte and operated under Ar. Similar to the signature of

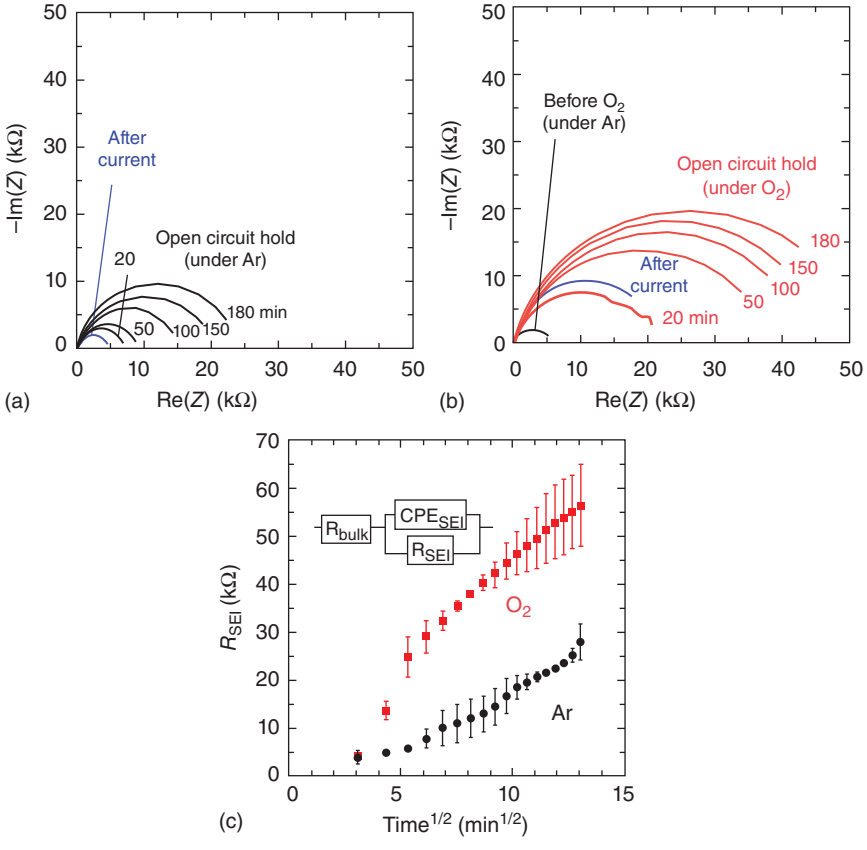

Figure 11.12 (a) Nyquist plots for a Mg/Mg cell containing MACC/DME electrolyte under Ar at various times during an open circuit (OC) hold (black) and after passing 0.075 mAh cm^{-2} through the cell at 0.05 mA cm^{-2} (blue). (b) Nyquist plots for a Mg/Mg cell using MACC/DME before O_2 exposure (black), under O_2 at various times after O_2 exposure during an OC hold (red), and after passing 0.075 mAh cm^{-2} (blue). (c) Equivalent-circuit model fit values of R_{SEI} during OC holds for Mg/Mg cells under Ar (black circles) and under O_2 (red squares).

solid-electrolyte interphase (SEI) formation in Li-ion-battery negative electrodes, the magnitude of the interfacial impedance increases as a function of time. After a hold at open circuit, 0.075 mAh cm^{-2} of charge was passed through the cell, and the impedance decreased substantially, suggesting electrochemically driven dissolution of an SEI-like layer from the Mg electrode surfaces. Similar studies show that Mg surfaces were reactivated after electrochemical polarization with a noncarbonated Mg electrolyte [93].

Figure 11.12b shows Nyquist plots for a symmetric Mg/Mg cell with MACC/DME electrolyte and operated under O_2. Exposure to O_2 accelerates the impedance increase. A subsequent passage of 0.075 mAh cm^{-2} at 0.05 mA cm^{-2} results in an impedance decrease, but the cell does not return to its state before O_2 exposure.

To quantify the effects of O_2 exposure, an equivalent-circuit model (ECM), illustrated in Figure 11.12c, was used to fit the EIS data gathered from both the Ar- and O_2-exposed Mg/Mg cells. In the ECM, R_{bulk}, R_{SEI}, and CPE_{SEI} represent the bulk resistance associated with the electrolyte, the Mg electrode's interfacial resistance, and the equivalent capacitance, respectively. Figure 11.12c shows how R_{SEI} varies with respect to the square root of time for Mg/Mg–MACC/DME cells under Ar and O_2. Notably, R_{SEI} increases with time under both Ar and O_2 atmospheres. Nevertheless, the cell exposed to O_2 exhibits a more rapid rate of increase and higher overall interfacial resistance, possibly due to oxidation of the Mg surface caused by the presence of O_2.

The evolution of R_{bulk}, which is associated with the resistance of the electrolyte and given by the high-frequency intercept of the Nyquist curve with the real axis, was investigated to gain insight into the relative stability of MACC and Grignard electrolytes under O_2. Comparison experiments, similar to those shown in Figure 11.12b, were performed on a Mg/Mg cell using the modified Grignard electrolyte. As shown in Figure 11.13, the rate of increase and the absolute value of R_{bulk} were both larger for the modified Grignard electrolyte than for MACC/DME. Lower R_{bulk} values for MACC/DME confirm the earlier

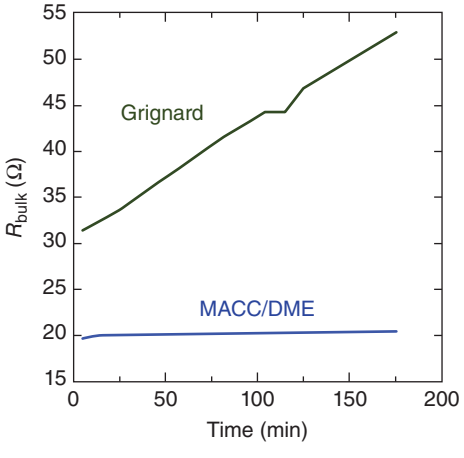

Figure 11.13 Variation of R_{bulk} with time for Mg/Mg cells exposed to O_2 using MACC/DME (blue) and modified Grignard (green) electrolytes.

mentioned higher conductivity of MACC/DME. Furthermore, the lower rate of increase for R_{bulk} suggests that MACC/DME is more stable with respect to O_2 exposure than the Grignard electrolyte.

Along with molecular O_2, the presence of O_2^- ions formed during cell discharge may intensify the oxidizing environment, further decomposing electrolytes [58, 68, 94]. Stability in the presence of O_2 and its electrochemical products appears to be at least as important as electrochemical stability against oxidation by the positive electrode. These effects are illustrated by the full Mg/O_2 cell EIS data shown in Figure 11.14.

Upon discharge of the full Mg/O_2 cell (Figure 11.14, blue and light blue curves), a second depressed semicircle in the Nyquist plot appeared, which likely owes to the formation of the discharge product layer. Similar EIS data (showing a new semicircle after discharge) have been observed previously during discharge of Li/O_2 cells [95].

An augmented ECM (Figure 11.14, top) containing an additional circuit element (parallel CPE_{prod}, R_{prod}) was used to model EIS data during and after discharge. Here, CPE_{prod} and R_{prod} represent the equivalent capacitance and resistance associated with the discharge-product layer. This layer's characteristic frequency is 4.40 MHz, with equivalent capacitance on the order of 1 pF. Both of these features point to the presence of a solid/liquid interface [96]. Figure 11.14 also highlights that the size of the new semicircle (which scales as R_{prod}) correlates with the depth of discharge.

In conclusion, EIS is a powerful tool that can be used to probe the interfaces in a Mg/O_2 battery as a function of time and charge state. The EIS data presented here has illustrated the changes in resistance associated with electrolyte decomposition, formation of an SEI-like layer on the Mg anode, and growth of the discharge product on the cathode.

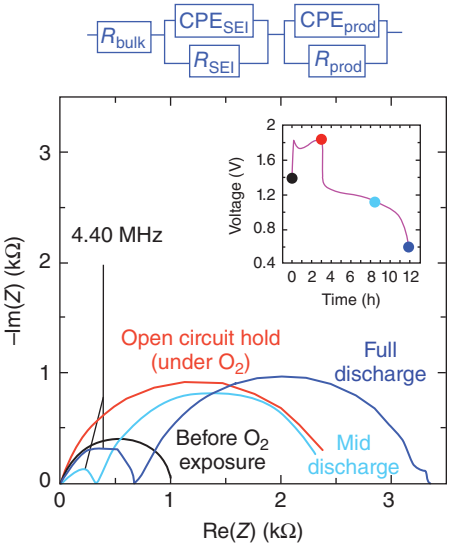

Figure 11.14 Electrochemical impedance spectra for a Mg/O_2 cell using MACC/DME electrolyte before O_2 exposure (black), after OC hold under O_2 (red), middischarge (light blue), and after discharge (blue). The inset indicates the stage of (pre)discharge at which the EIS data was measured. The ECM used to model the spectra is shown above.

11.3 Computational Studies of Mg/O_2 Batteries

In addition to the experimental studies described above, density functional theory calculations were used to characterize the reaction mechanisms and transport properties of the two primary discharge phases, MgO and MgO_2 [97, 98].

11.3.1 Calculation of Thermodynamic Overpotentials

Experiments have identified magnesium oxide (MgO) as one of the discharge products in nonaqueous Mg/O_2 cells [57, 70, 83]. Discharge voltages of approximately 1.2 V reported for these cells are well below the expected (theoretical) voltage of 2.95 V. An additional complication associated with an MgO discharge product is that MgO is considered electrochemically irreversible at ambient temperatures and practical voltages without the aid of a redox mediator [70, 83, 99]. In contrast, the analogous Li/O_2 system, it is well established that cells that discharge to lithium peroxide can be recharged with moderate voltages, while those that form lithium oxide cannot [100]. Therefore, a potentially more desirable discharge product in a Mg/O_2 cell may be magnesium peroxide (MgO_2). Clarifying the reaction mechanisms and energetics of discharge and charge for both of these compounds will assist in identifying strategies for improving performance.

The following reactions at the cathode are expected to govern the operation of a Mg/O_2 battery:

$$Mg^{2+} + 2e^- + \frac{1}{2}O_2 \rightleftharpoons MgO, \quad U_0 = 2.95\text{V}$$

$$Mg^{2+} + 2e^- + O_2 \rightleftharpoons MgO_2, \quad U_0 = 2.94\text{V}$$

During discharge, two electrons and a Mg^{2+} cation from the negative electrode react with oxygen at the positive electrode to form either MgO or MgO_2. During recharge, the reverse occurs and the solid discharge product is decomposed. The above theoretical cell potentials, U_0, are determined from the experimental Gibbs free energy of formation: $\Delta G_f^0(\text{MgO}) = -568.9\,\text{kJ mol}^{-1}$ and $\Delta G_f^0(\text{MgO}_2) = -567.8\,\text{kJ mol}^{-1}$ [101, 102]. A third possible discharge product is magnesium superoxide, $Mg(O_2)_2$. However, its thermal decomposition temperature was reported at −30 °C [103], making it unlikely to be a discharge product in Mg/O_2 batteries at room temperature. MgO_2 can be synthesized by treating MgO with hydrogen peroxide [104] or using an aqueous solution of magnesium hydroxide and hydrogen peroxide [105].

MgO adopts the rock salt crystal structure with each oxygen atom being coordinated by eight magnesium atoms (Figure 11.15a). Each oxygen atom has a formal oxidation number of 2^-. In MgO_2, each oxygen dimer is coordinated by eight magnesium atoms (Figure 11.15b), resulting in a charge of 2^- per dimer (O_2^{2-}). Although some preliminary crystallographic data for $Mg(O_2)_2$ is available [106], its crystal structure is not known.

Our calculations assume that discharge and charge occur via sequential adsorption/desorption reactions of Mg and oxygen at the surface of the discharge product. Moreover, the oxygen O_2^0 consumed to form the oxide (O^{2-}) or peroxide (O_2^{2-}) may be reduced in a single-step or multistep mechanism.

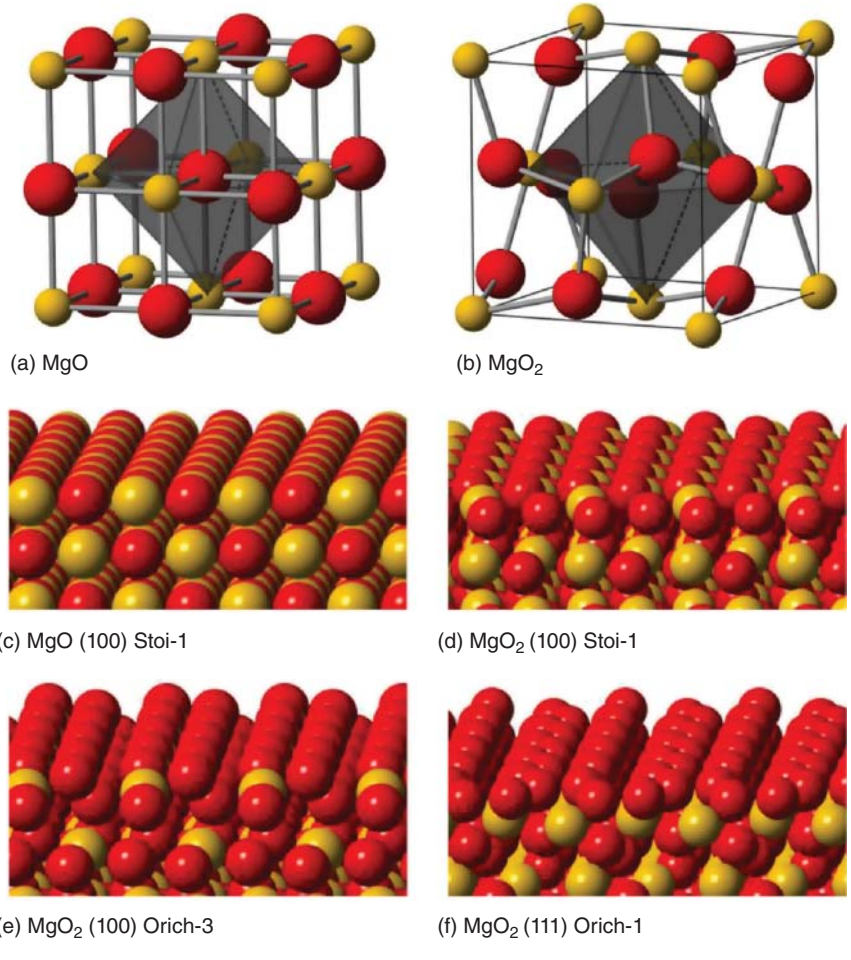

Figure 11.15 The rock salt crystal structure of MgO (a) and the pyrite crystal structure of MgO_2 (b). Most stable surface terminations of MgO and MgO_2 (c–f). Red indicates oxygen atoms, and yellow indicates magnesium atoms.

All calculations were performed using the Vienna *ab initio* simulation package (VASP code) [107–110].

Modeling the surface growth of MgO and MgO_2 requires knowledge of the low energy surface facets of these compounds. The two lowest energy surfaces for MgO are the stoichiometric (100) and (110) planes, with energies of 55 and 137 meV $Å^{-2}$, respectively. For MgO_2, there are three stable surfaces: the stoichiometric (100) surface and two oxygen-rich (100) and (111) surfaces with energies of 52, 49, and 57 meV $Å^{-2}$, respectively. Elementary reaction mechanisms were modeled on these four low energy surfaces, depicted in Figure 11.15c–f.

The (100) surfaces were modeled using a 2×2 expansion of the conventional surface unit cell; the (111) surface was modeled with a 2×1 expansion. For both MgO and MgO_2, each surface layer comprises eight formula units; thus,

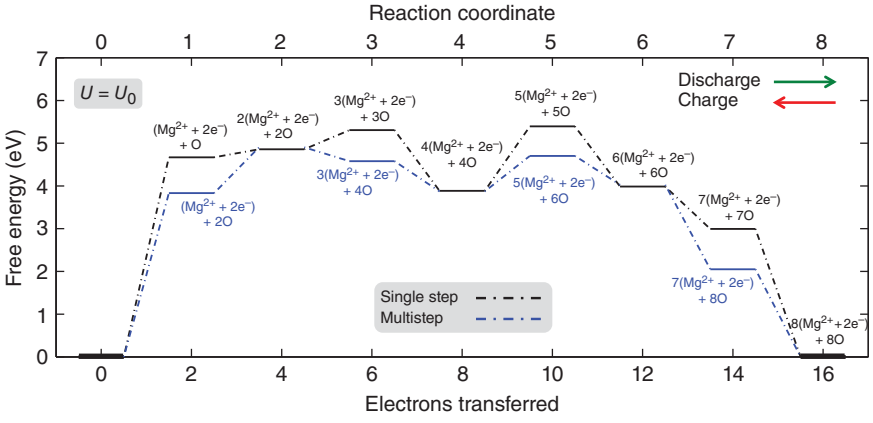

Figure 11.16 Calculated free energy diagram for the discharge and charging of an Mg/O_2 cell on a MgO (100) surface. The black line refers to the single-step pathway, and the blue line refers to the multistep pathway (with peroxide intermediates). The identity of the surface adsorbed species is indicated with text. Energies are plotted assuming the application of a potential, U, equal to the theoretical cell potential, $U = U_0$.

a complete discharge reaction pathway (equivalent to growing a new layer of discharge product) consists of the sequential deposition of 8 Mg and oxygen atoms for MgO or 8 Mg and 16 oxygen atoms for MgO_2.

The calculated energetics associated with two plausible reaction mechanisms (corresponding to single-step and multistep reduction) on the MgO (100) surface are shown in Figure 11.16. The single-step mechanism

$$(Mg^{2+} + 2e^-) + \frac{1}{2}O_2 + * \rightleftharpoons MgO^*$$

reduces oxygen in a single reaction step and is shown by the black line. The multistep mechanism involves a surface adsorbed oxygen intermediate, magnesium peroxide ($MgO_2{}^*$), followed by an additional deposition of a Mg atom. This pathway is shown with the blue line and occurs via the following two reactions:

$$(Mg^{2+} + 2e^-) + O_2 + * \rightleftharpoons MgO_2{}^*$$
$$MgO_2{}^* + (Mg^{2+} + 2e^-) \rightleftharpoons 2MgO^*$$

here a lone asterisk denotes a surface site, while the superscripted asterisk indicates a surface adsorbed species.

The forward direction of the preceding reactions corresponds to the discharge process, where the reactants are Mg and oxygen. The reverse reaction direction corresponds to charging. Consequently, the reaction pathway diagrams are read left to right for discharge and right to left for charging.

The reaction energy diagrams (Figures 11.16 and 11.17) are plotted with an applied voltage, U, equal to the theoretical voltage, U_0. Under these conditions, equilibrium between reactants and products exists and is indicated by a zero reaction energy, $\Delta G_{rxn} = G_{products} - G_{reactants}$. Thus a positive reaction energy between elementary discharge/deposition steps appears as an uphill step in energy and is proportional to the thermodynamic overpotential, $\Delta G_{rxn} = \eta e \nu$. Here, η is the

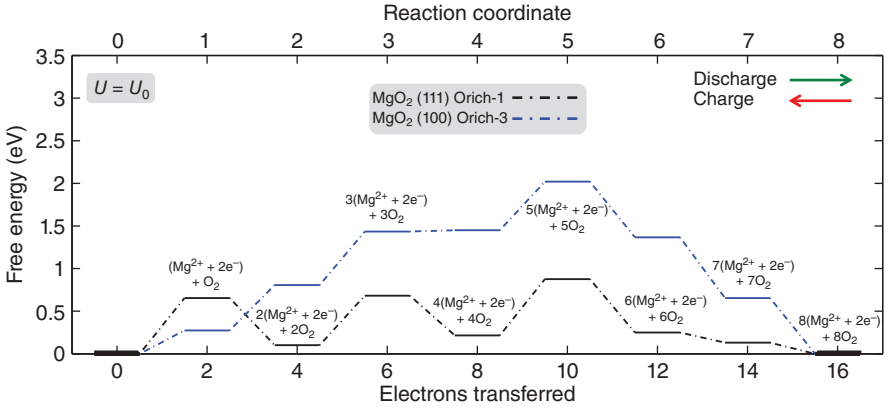

Figure 11.17 Calculated free energy diagram for discharge and charge of an Mg/O_2 cell for single-step reactions occurring on the oxygen-rich MgO_2 (111) *Orich-1* (black curve) and MgO_2 (100) *Orich-3* (blue curve) surfaces. The identity of the surface adsorbed species is indicated with text. Energies are plotted assuming the application of a potential, U, equal to the theoretical cell potential, $U = U_0$. (Note that the maximum value for the ordinate (3.5 eV) used in this plot is half the value used in Figure 11.16.)

thermodynamic overpotential [111, 112], e is the charge of an electron, and ν is the number of electrons transferred. For discharge, the reaction pathway shown in Figure 11.16 will not proceed unless the voltage is reduced by the amount equal to the discharge overpotential, $\eta^{\text{discharge}}$. Similarly, for charge the reaction pathway will not proceed unless the voltage is increased by the amount equal to the charging overpotential, η^{charge}. It is the largest respective *uphill* step for discharge and charge that determines the overpotential.

Returning to the calculated reaction pathway for the formation of MgO (100) (shown in Figure 11.16), the so-called *potential determining step* corresponds to the largest uphill step. This is the first step in the reaction, i.e. the reaction of Mg and oxygen on an empty terrace of MgO (100). This step results in an overpotential of 2.25 V, which is equivalent to a low discharge voltage of 0.70 V. In contrast, the multistep mechanism results in a lower overpotential of 1.8 V, equivalent to a discharge voltage of 1.15 V. (This reaction step is shown by the (lower) blue line at reaction coordinate 1 in Figure 11.16.) Examination of the remainder of the reaction pathway for both single- and multistep mechanisms indicates that it is more favorable to reduce oxygen via the multistep pathway, which involves the formation of a peroxide intermediate. Likewise, upon charge it is energetically favorable to first desorb a Mg atom followed by the desorption of a MgO_2* species. The overpotentials and limiting potentials for discharge and charge are summarized in Table 11.1.

Next we consider a Mg/O_2 battery that discharges to magnesium peroxide (MgO_2). Here two plausible reaction mechanisms are considered. First, the single-step mechanism,

$$(Mg^{2+} + 2e^-) + O_2 + * \rightleftharpoons MgO_2{}^*$$

Table 11.1 Calculated limiting potentials, thermodynamic overpotentials, and efficiencies associated with various discharge and charge reactions in an Mg/O_2 cell.

Discharge product, surface, and reaction mechanism	Limiting potential (V)		Overpotential (V)		Voltaic efficiency (%)
	Discharge	Charge	Discharge	Charge	
MgO (100) stoi (single step)	0.70	4.45	2.25	1.50	16
MgO (100) stoi (multistep)	1.15	3.98	1.80	1.03	29
MgO_2 (100) stoi (single step)	0.92	4.69	2.02	1.75	20
MgO_2 (100) stoi (multistep)	1.31	4.04	1.63	1.10	33
MgO_2 (111) Orich-1 (single step)	2.76 (2.61)	3.01 (3.25)	0.18 (0.33)	0.07 (0.31)	92 (80)
MgO_2 (100) Orich-3 (single step)	2.83 (2.63)	3.27 (3.29)	0.11 (0.31)	0.33 (0.35)	87 (80)
Li_2O_2 [92]	—	—	0.35, 0.68	0.20, 0.40	—

Values in regular text refer to terrace-site reactions; values in parentheses refer to nonterrace reactions, which are limiting only for the superoxide terminated surfaces, Orich-1 and Orich-3. The voltaic efficiency is defined as U^{dis}/U^{chg}.

reduces oxygen in a single reaction. In contrast, the second reaction mechanism is a multistep process involving a surface adsorbed superoxide $Mg(O_2)_2{}^*$, followed by an additional deposition of a Mg ion and electrons:

$$(Mg^{2+} + 2e^-) + 2O_2 + * \rightleftharpoons Mg(O_2)_2{}^* \tag{11.5}$$

$$Mg(O_2)_2{}^* + (Mg^{2+} + 2e^-) \rightleftharpoons 2MgO_2{}^*. \tag{11.6}$$

The reaction pathway on the stoichiometric MgO_2 (100) surface is reported in Ref. [97]. On that surface the formation of MgO_2 occurs more readily via the multistep mechanism.

The two lowest energy surfaces of MgO_2 are oxygen-rich terminations (Figure 11.15e,f) with a O:Mg ratio of 4 : 1. On these surfaces each oxygen dimer exists in a superoxide-like charge state with a Bader charge of approximately −1, a bond length of 1.35 Å, and a nonzero magnetic moment. This contrasts with the MgO_2 stoichiometric (100) surface, where each surface oxygen dimer has a Bader charge of approximately −2, a bond length of 1.51 Å, and no magnetic moment. Reaction energies for the superoxide terminated surfaces were evaluated using a single-step mechanism because these surfaces already exist in a charge state for O_2 that is its least-reduced configuration.

The elementary reaction steps associated with the formation of a complete MgO_2 surface layer on an initial pristine MgO_2 surface are shown in Figure 11.17. Importantly, the calculated overpotentials are significantly smaller than the

overpotentials on the MgO (100) surface. More specifically, the discharge and charge overpotentials for the Orich-1 surface are 0.33 and 0.31 V, respectively. The potential limiting steps (i.e. largest uphill steps) in the reaction occur at step 4 → 5 for discharge and at 6 → 5 for charge. Similarly, discharge and charge overpotentials for the Orich-3 surface are relatively low, 0.31 and 0.35 V, respectively. For this surface, the potential limiting steps occur at step 2 → 3 for discharge and at 7 → 6 for charge. The location of the potential limiting steps on the O-rich MgO_2 surfaces differs from the behavior on MgO; in the latter case the potential limiting steps occur on terrace sites.

Due to the high concentration of terrace-based sites, it has been suggested [92, 113] that these sites are the most important contributor to overpotentials in a practical cell. Using the limiting potentials from the terrace-based sites alone, even smaller overpotentials are observed, with efficiencies approaching 90%, shown in Table 11.2.

The overpotential calculations suggest that discharge and charge reactions in an Mg/O_2 cell are much more efficient when they occur on superoxide surfaces, which are expected to appear on the surface of a MgO_2 crystallite [97]. The experiments using the modified Grignard electrolyte (described above) are in agreement with this result: this cell exhibited a mixed MgO + MgO_2 discharge product [57], with smaller overpotentials and higher rechargeability than are observed in MgO-based cells [70, 83]. Consequently, biasing the discharge product toward the formation of MgO_2 is suggested as a strategy to enhance the performance of Mg/O_2 batteries.

11.3.2 Charge Transport in Mg/O_2 Discharge Products

Achieving high energy density and efficiency in metal–oxygen batteries requires that the discharge product grows (during discharge) and subsequently decomposes (during recharge) at voltages near the theoretical voltage. So far, Mg/O_2 batteries have shown limited cell capacity and reversibility [57, 70, 83]. In analogous Li/O_2 cells, limited capacity (or *sudden death*) during discharge and high charging overpotentials have been attributed to the insulating nature of the discharge product [2, 69, 100, 114–118]. The low electrical conductivity of M–O_2

Table 11.2 Formation energies and migration barriers for various defects in MgO and MgO_2.

	Formation energy (E_f)				Migration barrier (E_b)	
	Schottky	Cation Frenkel	Anion Frenkel	Selected point defects	Polaron	V_{Mg}^{2-}
MgO	6.91	10.05	13.8	2.23 (V_{Mg}^{2-} or p^+)	0.11 (p^+)	2.20
MgO_2	8.33	9.78	[a]10.24, [b]12.16	1.82 (p^+ or p^-)	0.56 (p^+) 1.76 (p^-)	—

Schottky and Frenkel defects are comprised of a pair of point defects; their formation energies are reported on a per-pair basis.

a) (V_O^+, O_I^-).

b) (V_O^{2+}, O_I^{2-}).

(M = K, Na, Li, Mg) discharge products may be a universal limitation that must be overcome to achieve efficient metal–oxygen batteries. Understanding the charge transport mechanisms in these compounds is an important first step in devising strategies to address these limitations.

The equilibrium conductivity of MgO and MgO_2 arising from the presence of point defects has been reported in an earlier study [98] and is summarized here. Defect formation energy and mobility calculations were performed using the VASP code [107–110]. The Heyd–Scuseria–Ernzerhof (HSE) hybrid functional was used with a fraction of exact exchange tuned ($\alpha = 0.42$) to reproduce the bandgap obtained from GW calculations [119–122]. This *HSEα* functional predicts a bandgap of 7.8 and 7.9 eV for MgO and MgO_2, respectively.

The formation energy of intrinsic defects for MgO and MgO_2 are shown in Figure 11.18. Each line corresponds to a defect type: magnesium vacancies (blue lines), magnesium interstitials (blue-dashed lines), oxygen vacancies (red lines), oxygen interstitials (red-dashed lines), and dioxygen vacancies (green lines); hole and electron polarons are shown in black. The slope of each line corresponds to its respective charge state: values of −2, −1, 0, +1, and +2 were considered. The dashed line indicates the position of the Fermi level, which is determined by charge neutrality among all defects.

For MgO, the defects with the lowest formation energy are the hole polaron (p^+) and doubly negative Mg vacancy (V_{Mg}^{2-}), shown in Figure 11.18a. The hole polaron is comprised of the absence of one electron on an oxygen site and its resulting local lattice distortion. The magnesium to oxygen distance near the p^+ is slightly elongated from 2.1 Å (in bulk) to 2.18–2.25 Å. The elongation of these bonds is due to the weaker electrostatic interaction from the less negatively

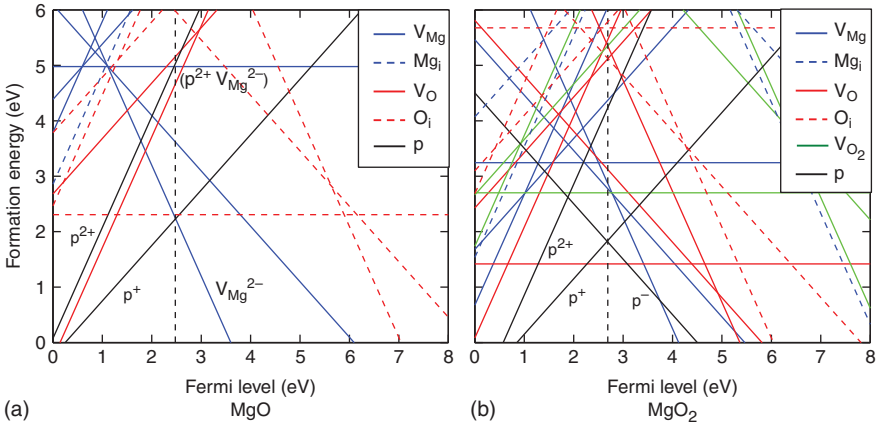

Figure 11.18 Formation energies of intrinsic defects in (a) MgO and (b) MgO_2 calculated using the HSE*α* functional. Magnesium vacancies (V_{Mg}) are depicted using blue lines, magnesium interstitials (Mg_I) with blue-dashed lines, oxygen vacancies (V_O) with red lines, oxygen interstitials (O_I) with red-dashed lines, and oxygen divacancies (V_{O_2}) with green lines. Hole and electron polarons are shown in black. The slope of each line corresponds to its respective charge state; values of −2, −1, 0, +1, and +2 were considered (positive slopes correspond to defects with positive charges). The dashed line indicates the position of the Fermi level.

charged oxygen ion. The formation energy of the polaron (and Mg vacancy) is high, 2.23 eV, resulting in a low equilibrium concentration of 1×10^{-15} cm^{-3}.

In the case of MgO_2, the defects with the lowest formation energy are the hole polaron (p^+) and electron polaron (p^-), shown in Figure 11.18b. Here the polaron is formed by the addition or absence of charge on an oxygen dimer (O_2^{2-}). Similar to the polaron in MgO, the local magnesium–oxygen bond length is elongated (for the hole) or contracted (for the electron). Additionally, the oxygen dimer bond distance is contracted from 1.45 Å (in bulk) to 1.30 Å for the hole polaron and elongated to 2.07 Å for the electron polaron. The formation energy of the hole and electron polaron is also high, 1.82 eV, resulting in low equilibrium concentrations of 6×10^{-9} cm^{-3}.

Schottky and Frenkel defects in MgO have been studied by several other researchers (see Table 2 of Ref. [[98]]). A Schottky defect is a cation (Mg^{2+}) and anion (O^{2-}) vacancy pair; a Frenkel defect is a vacancy-interstitial pair. The formation energies for these defects in MgO and MgO_2 were calculated with the HSEα ($\alpha = 0.42$) functional. Formation energies for Schottky defects and for cation and anion Frenkel defects are 6.91, 10.05, and 13.8 eV in MgO, respectively. In regard to MgO, prior studies using a variety of computational methods report that Schottky defects fall in the range 5–9 eV, cation Frenkel defects form with energies of 10–14 eV, and anion Frenkel defects occur at 12–15 eV (see Ref. [[98]]). Experimental measurements of the Schottky defect formation energy range from 5 to 7 eV [123].

The calculated Schottky and Frenkel defect formation energies in MgO_2 are similar in magnitude to those in MgO. For Schottky defects in MgO_2, the anion vacancy is an oxygen dimer (O_2^{2-}). For anion Frenkel defects, two interstitials were considered, O_I^- and O_I^{2-}. The calculated formation energies for Schottky defects and cation and anion Frenkel defects are 8.33, 9.78, and 10.24 eV in MgO_2, respectively. A summary of the calculated defect formation energies is given in Table 11.2. The high formation energies associated with these defects suggest that their equilibrium concentrations are negligible.

The charged defects with the lowest formation energies (highest concentrations) are expected to be the dominant species responsible for electrical conduction. In order to estimate the equilibrium conductivity, the mobility, and hence the migration barrier of each species, needs to be known. The migration barriers for the lowest formation energy defects in MgO and MgO_2 were calculated using the nudged elastic band (NEB) method [124, 125]. These species and their respective barriers are shown in Table 11.2 and Figure 11.19. For MgO, there is a large difference in the migration barrier of the hole polaron (0.11 eV) and Mg vacancy (2.20 eV). This results in a difference in mobility of 35 orders of magnitude, as shown in Table 11.3. As will be discussed later, a consequence of these barrier differences is that the Mg vacancy is effectively immobile at low temperatures, leading to nonequilibrium effects.

For MgO_2, the migration barrier of the electron polaron (1.76 eV) is nearly three times that of the hole polaron (0.56 eV). This trend is also observed in other peroxides of relevance for metal–oxygen batteries, namely, Li_2O_2 and Na_2O_2. For Li_2O_2, Garcia-Lastra et al. [126] found in-plane/out-of-plane barriers for p^+ migration of 0.39/0.48 eV and 1.41/1.47 eV for p^- migration; Radin and Siegel

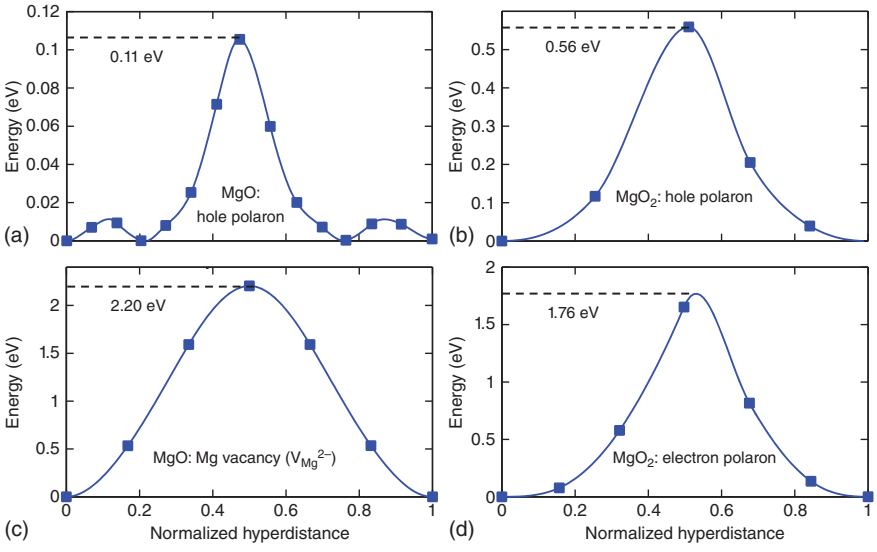

Figure 11.19 Migration energy barriers of dominant defects in MgO and MgO_2 calculated using the NEB method. (a) Hole polaron and (c) magnesium vacancy (V_{Mg}^{2-}) in MgO. (b) Hole polaron and (d) electron polaron in MgO_2.

Table 11.3 Calculated diffusion coefficient, mobility, and conductivity of dominant defects in MgO and MgO_2.

Compound	Diffusion coefficient, D ($cm^2\ s^{-1}$)	Mobility, μ $(cm^2(Vs)^{-1})$	Conductivity, σ ($S\ cm^{-1}$)
MgO (p^+)	1×10^{-4}	6×10^{-3}	3×10^{-36}
MgO (V_{Mg}^{2-})	1×10^{-39}	4×10^{-38}	1×10^{-71}
MgO_2 (p^+)	4×10^{-12}	1×10^{-10}	3×10^{-37}
MgO_2 (p^-)	2×10^{-32}	6×10^{-31}	7×10^{-58}
Li_2O_2 (p^+)	9×10^{-10}	—	5×10^{-20}
Na_2O_2 (p^+)	—	—	1×10^{-20}
NaO_2 (p^-)	—	—	1×10^{-19}
NaO_2 ($V_{O_2}^{+}$)	6×10^{-7}	—	4×10^{-9}

Data from literature for Li_2O_2, Na_2O_2, and NaO_2 are included for comparison [115, 127].

[115] reported 0.42/0.71 for in-plane/out-of-plane migration of p^+. For Na_2O_2, Yang and Siegel [127] reported 0.47/0.62 eV for in-plane/out-of-plane migration of p^+. This suggests the transport of electronic species in peroxides is similar regardless of the cation, with the hole polaron being considerably more mobile than the electron polaron.

The calculated diffusion coefficients, mobilities, and conductivities of the four predominant charge carriers in MgO and MgO_2 at room temperature are shown in Table 11.3. For comparison data reported for Li_2O_2 and Na_2O_2 are

also shown [115, 127]. The conductivity of MgO (3×10^{-36} S cm^{-1}) and MgO_2 (3×10^{-37} S cm^{-1}) are very low and similar in magnitude. This suggests sluggish charge transport through these phases would be a limiting factor for battery performance.

However, it is important to recognize that the calculated conductivities likely represent a lower bound to the conductivity, since they assume equilibrium concentrations are achieved at room temperature. In the case of MgO, establishing an equilibrium vacancy concentration requires atoms to be transported to vacancy sources or sinks over large distances, such as from bulk regions to the surface. This process can be very slow, leading to nonequilibrium concentrations of ionic defects being *frozen-in* at low temperatures. Most crystal samples used in conductivity experiments are prepared at elevated temperatures or heat treated; consequently, the concentration of ionic defects present in low temperature measurements is fixed at those (high) temperatures. For many oxides, equilibrium is attained only above 400–800 °C [128]. The distinction between high and low temperature defect chemistry in other compounds has been thoroughly noted elsewhere [128–133].

Despite many years of study, the mechanism of electronic transport in MgO remains a matter of debate [134, 135]. The calculations described here present an opportunity to clarify these mechanisms. Most experimental studies are reported at temperatures above 1000 K. In this high temperature regime, the calculated conductivity agrees well with experimental data. For example, experimental studies suggest an Arrhenius energy of 2.4 eV, while the calculated Arrhenius energy is 2.34 eV [98]. The conductivity is conventionally described in terms of the Arrhenius energy, W, according to the expression $\sigma = \sigma_0 \exp(-W/k_B T)$. Where W is the sum $(E_f + E_b)$ of the formation and migration energies of the charge carrier, k_B is the Boltzmann constant, and T is the absolute temperature. The agreement between experiment and computation is illustrated in Figure 11.20, where the red line shows the calculated conductivity, while the red oval overlays the experimental data. The agreement between experiment and

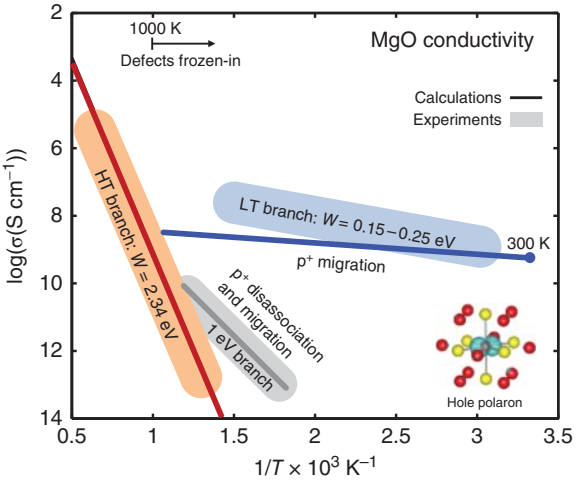

Figure 11.20 Arrhenius plot of the conductivity of MgO, illustrating the three Arrhenius branches reported in experiments: (red) high temperature (HT) branch, (blue) low temperature (LT) branch, and (gray) 1 eV branch.

calculation suggest that conduction is due to the formation and migration of hole polarons and Mg vacancies.

Below approximately 1000 K it has been noted that the conductivity is temperature history dependent [134, 136, 137]. At these temperatures two additional Arrhenius branches are reported in the literature: a low temperature branch and a 1 eV branch [134, 136, 138]. Upon cooling from the high temperature branch ($W = 2.4$ eV), a low temperature branch with an Arrhenius energy of 0.15–0.25 eV is observed. We speculate this branch results from a nonequilibrium concentration of carriers that are frozen-in during cooling near a temperature of approximately 1000 K. The Arrhenius energy is determined by the migration barrier of hole polarons, which was calculated to be 0.11 eV [98], this is in good agreement with experimental data of 0.15–0.25 eV [134, 136, 138]. The calculated conductivity is shown in Figure 11.20 (blue line) and is determined using the equilibrium concentration of hole polarons at 1000 K, 6.2×10^{11} cm^{-3}. The calculated conductivity is in good agreement with the experimental data, visualized as a blue oval.

The third reproducible branch in the MgO conductivity data is obtained upon heating near 800 K [134–136]. Batllo et al. [139] argued that this 1 eV branch was due to the disassociation of holes bound to doubly negative Mg vacancies. This hypothesis was supported by anomalies in the magnetic susceptibility and charge distribution data. In this process two hole polarons disassociate from a neutral Mg vacancy, leaving behind a doubly negative Mg vacancy. The dissociation (i.e. formation) energy for the first p^+ is 0.87 eV, and the second p^+ has a similar value of 0.85 eV. Combined with the low migration barrier of the hole polaron, 0.11 eV, the calculated Arrhenius energy is 0.97 eV (gray line in Figure 11.20). This value is in remarkable agreement with the measured Arrhenius energy of 1 eV. This result supports the hypothesis of Batllo et al. that the 1 eV branch is due to the disassociation and migration of hole polarons bound to Mg vacancies.

The preceding discussion suggests that the low equilibrium carrier concentration predicted for MgO and MgO_2 is unlikely to be achieved at the low temperatures typical of battery operation. Instead, nonequilibrium concentrations are expected to dominate. These concentrations will be influenced by how rapidly the MgO + MgO_2 discharge product is formed (i.e. discharge rate) and by the incorporation of species from the electrolyte into the discharge phase. In principle, aliovalent impurities intentionally added to the electrolyte could enhance the concentration of carriers. For example, in both MgO and MgO_2 hole polarons have substantially higher mobility than their charge compensating species. The high mobility of hole polarons could be exploited by the substitution of monovalent impurities (such as Li) on Mg sites, which would artificially increase the concentration of these mobile carriers.

11.4 Concluding Remarks

This chapter has described some of the early experimental and computational studies of Mg/O_2 batteries. The Mg/O_2 chemistry is an enticing system because it combines the capacity advantages of an air-breathing cathode with those of

a multivalent Mg metal anode while allowing for lower cost and higher safety compared to Li analogs. Nevertheless, relatively few experimental studies of this system have been reported, and these studies demonstrate performance that is far from ideal: high overpotentials and limited cycleability are commonly observed. These reports illustrate the challenges that remain before the benefits of the Mg/O_2 chemistry can be realized in a practical cell.

Recent progress in the Mg/O_2 system includes the demonstration of high discharge capacities and the potential for reversibility. Unfortunately, these two desirable features have thus far been demonstrated only separately; no one cell chemistry has yet shown the ability to yield high energy densities and efficient rechargeability simultaneously.

Looking to the future, there are reasons to be optimistic about the development of Mg/O_2 batteries. First, the global emphasis given to the analogous Li/O_2 and Na/O_2 systems will likely yield insights that apply equally well to the Mg/O_2 chemistry. For example, benefits associated with the use of redox mediators in the alkali-metal-based systems should be transferrable to the Mg/O_2 system. A similar technology spillover is anticipated from the growing interest in Mg-ion batteries and the concurrent development of Mg-ion electrolytes. New Mg-ion electrolytes that foster efficient plating and stripping from Mg negative electrodes should be assessed for their stability in the O_2-containing environments typical of Mg/O_2 cathodes.

References

1 Heywood, J. (1988). *Internal Combustion Engine Fundamentals*. McGraw-Hill.

2 Bruce, P.G., Freunberger, S.A., Hardwick, L.J., and Tarascon, J.-M. (2012). $Li–O_2$ and Li–S batteries with high energy storage. *Nat. Mater.* 11: 19–29.

3 Abraham, K.M. and Jiang, Z. (1996). A polymer electrolyte-based rechargeable lithium/oxygen battery. *J. Electrochem. Soc.* 143: 1–5.

4 Hartmann, P., Bender, C.L., Vračar, M. et al. (2013). A rechargeable room-temperature sodium superoxide (NaO_2) battery. *Nat. Mater.* 12: 228–232.

5 Ren, X. and Wu, Y. (2013). A low-overpotential potassium–oxygen battery based on potassium superoxide. *J. Am. Chem. Soc.* 135: 2923–2926.

6 Chen, C.H. and Amine, K. (2001). Ionic conductivity, lithium insertion and extraction of lanthanum lithium titanate. *Solid State Ionics* 144: 51–57.

7 Zu, C.-X. and Li, H. (2011). Thermodynamic analysis on energy densities of batteries. *Energy Environ. Sci.* 4: 2614–2624.

8 Abraham, K.M. (2008). A brief history of non-aqueous metal–air batteries. *ECS Trans.* 3: 67–71.

9 Chakkaravarthy, C., Waheed, A.K.A., and Udupa, H.V.K. (1981). Zinc–air alkaline batteries – a review. *J. Power Sources* 6: 203–228.

10 Caramia, V. and Bozzini, B. (2014). Materials science aspects of zinc–air batteries: a review. *Mater. Renew. Sustain. Energy* 3: 28.

11 Hamlen, R.P., Jerabek, E.C., Ruzzo, J.C., and Siwek, E.G. (1969). Anodes for refuelable magnesium–air batteries. *J. Electrochem. Soc.* 116: 1588.

12 Sathynarayana, S. and Munichandraiah, N. (1981). A new magnesium–air cell for long-life applications. *J. Appl. Electrochem.* 11: 33–39.

13 Winther-Jensen, B., Gaadingwe, M., Macfarlane, D.R., and Forsyth, M. (2008). Control of magnesium interfacial reactions in aqueous electrolytes towards a biocompatible battery. *Electrochim. Acta* 53: 5881–5884.

14 Khoo, T., Somers, A., Torriero, A.A.J. et al. (2013). Discharge behaviour and interfacial properties of a magnesium battery incorporating trihexyl(tetradecyl)phosphonium based ionic liquid electrolytes. *Electrochim. Acta* 87: 701–708.

15 Khoo, T., Howlett, P.C., Tsagouria, M. et al. (2011). The potential for ionic liquid electrolytes to stabilise the magnesium interface for magnesium/air batteries. *Electrochim. Acta* 58: 583–588.

16 Ling, C., Banerjee, D., and Matsui, M. (2012). Study of the electrochemical deposition of Mg in the atomic level: why it prefers the non-dendritic morphology. *Electrochim. Acta* 76: 270–274.

17 Teranishi, T., Ishii, Y., Hayashi, H., and Kishimoto, A. (2016). Lithium ion conductivity of oriented $Li_{0.33}La_{0.56}TiO_3$ solid electrolyte films prepared by a sol–gel process. *Solid State Ionics* 284: 1–6.

18 Abhilash, K.P., Christopher Selvin, P., Nalini, B. et al. (2016). Study of the temperature dependent transport properties in nanocrystalline lithium lanthanum titanate for lithium ion batteries. *J. Phys. Chem. Solids* 91: 114–121.

19 MacFarlane, D.R., Tachikawa, N., Forsyth, M. et al. (2014). Energy applications of ionic liquids. *Energy Environ. Sci.* 7: 232.

20 Kar, M., Winther-Jensen, B., Forsyth, M., and MacFarlane, D.R. (2013). Chelating ionic liquids for reversible zinc electrochemistry. *Phys. Chem. Chem. Phys.* 15: 7191–7197.

21 Galiński, M., Lewandowski, A., and Stępniak, I. (2006). Ionic liquids as electrolytes. *Electrochim. Acta* 51: 5567–5580.

22 MacFarlane, D.R., Forsyth, M., Howlett, P.C. et al. (2016). Ionic liquids and their solid-state analogues as materials for energy generation and storage. *Nat. Rev. Mater.* 1: 15005.

23 Ohno, H. (2011). *Electrochemical Aspects of Ionic Liquids*. Wiley.

24 Brennecke, J.F. and Maginn, E.J. (2001). Ionic liquids: innovative fluids for chemical processing. *AIChE J.* 47: 2384–2389.

25 Lewandowski, A. and Świderska-Mocek, A. (2009). Ionic liquids as electrolytes for Li-ion batteries – an overview of electrochemical studies. *J. Power Sources* 194: 601–609.

26 Ishikawa, M., Sugimoto, T., Kikuta, M. et al. (2006). Pure ionic liquid electrolytes compatible with a graphitized carbon negative electrode in rechargeable lithium-ion batteries. *J. Power Sources* 162: 658–662.

27 Howlett, P.C., MacFarlane, D.R., and Hollenkamp, A.F. (2004). High lithium metal cycling efficiency in a room-temperature ionic liquid. *Electrochem. Solid-State Lett.* 7: A97.

28 Cui, Z.H., Fan, W.G., and Guo, X.X. (2013). Lithium–oxygen cells with ionic-liquid-based electrolytes and vertically aligned carbon nanotube cathodes. *J. Power Sources* 235: 251–255.

29 Yan, Y., Yin, Y.-X., Xin, S. et al. (2013). High-safety lithium–sulfur battery with prelithiated Si/C anode and ionic liquid electrolyte. *Electrochim. Acta* 91: 58–61.

30 Sun, X.-G., Wang, X., Mayes, R.T., and Dai, S. (2012). Lithium–sulfur batteries based on nitrogen-doped carbon and an ionic-liquid electrolyte. *ChemSusChem* 5: 2079–2085.

31 Yuan, L.X., Feng, J.K., Ai, X.P. et al. (2006). Improved dischargeability and reversibility of sulfur cathode in a novel ionic liquid electrolyte. *Electrochem. Commun.* 8: 610–614.

32 Zhao, Q., NuLi, Y., Nasiman, T. et al. (2012). Reversible deposition and dissolution of magnesium from imidazolium-based ionic liquids. *Int. J. Electrochem.* 2012: 1–8.

33 NuLi, Y., Yang, J., and Wang, P. (2006). Electrodeposition of magnesium film from $BMIMBF_4$ ionic liquid. *Appl. Surf. Sci.* 252: 8086–8090.

34 Feng, Z., NuLi, Y., Wang, J., and Yang, J. (2006). Study of key factors influencing electrochemical reversibility of magnesium deposition and dissolution. *J. Electrochem. Soc.* 153: C689.

35 NuLi, Y., Yang, J., Wang, J. et al. (2005). Electrochemical magnesium deposition and dissolution with high efficiency in ionic liquid. *Electrochem. Solid-State Lett.* 8: C166.

36 Wang, P., NuLi, Y., Yang, J., and Feng, Z. (2006). Mixed ionic liquids as electrolyte for reversible deposition and dissolution of magnesium. *Surf. Coatings Technol.* 201: 3783–3787.

37 Amir, N., Vestfrid, Y., Chusid, O. et al. (2007). Progress in nonaqueous magnesium electrochemistry. *J. Power Sources* 174: 1234–1240.

38 Cheek, G.T., O, Grady, W.E., El Abedin, S.Z. et al. (2008). Studies on the electrodeposition of magnesium in ionic liquids. *J. Electrochem. Soc.* 155: D91.

39 Shimamura, O., Yoshimoto, N., Matsumoto, M. et al. (2011). Electrochemical co-deposition of magnesium with lithium from quaternary ammonium-based ionic liquid. *J. Power Sources* 196: 1586–1588.

40 Gregory, T.D. (1990). Nonaqueous electrochemistry of magnesium. *J. Electrochem. Soc.* 137: 775.

41 Aurbach, D., Lu, Z., Schechter, A. et al. (2000). Prototype systems for rechargeable magnesium batteries. *Nature* 407: 724–727.

42 Lu, Z., Schechter, a., Moshkovich, M., and Aurbach, D. (1999). On the electrochemical behavior of magnesium electrodes in polar aprotic electrolyte solutions. *J. Electroanal. Chem.* 466: 203–217.

43 Doe, R.E., Han, R., Hwang, J. et al. (2014). Novel, electrolyte solutions comprising fully inorganic salts with high anodic stability for rechargeable magnesium batteries. *Chem. Commun.* 50: 243–245.

44 Liu, T., Shao, Y., Li, G. et al. (2014). A facile approach using $MgCl_2$ to formulate high performance Mg^{2+} electrolytes for rechargeable Mg batteries. *J. Mater. Chem. A* 2: 3430.

45 Yoshimoto, N., Matsumoto, M., Egashia, M., and Morita, M. (2010). Mixed electrolyte consisting of ethylmagnesiumbromide with ionic liquid for rechargeable magnesium electrode. *J. Power Sources* 195: 2096–2098.

46 Pan, B., Lau, K.-C., Vaughey, J.T. et al. (2017). Ionic liquid as an effective additive for rechargeable magnesium batteries. *J. Electrochem. Soc.* 164: A902–A906.

47 Kitada, A., Kang, Y., Uchimoto, Y., and Murase, K. (2013). Room-temperature electrodeposition of Mg metal from amide salts dissolved in glyme-ionic liquid mixture. *J. Electrochem. Soc.* 161: D102–D106.

48 Vardar, G., Sleightholme, A.E.S., Naruse, J. et al. (2014). Electrochemistry of magnesium electrolytes in ionic liquids for secondary batteries. *ACS Appl. Mater. Interfaces* 6: 18033–18039.

49 Lapidus, S.H., Rajput, N.N., Qu, X. et al. (2014). Solvation structure and energetics of electrolytes for multivalent energy storage. *Phys. Chem. Chem. Phys.* 16: 21941–21945.

50 Rajput, N.N., Qu, X., Sa, N. et al. (2015). The coupling between stability and ion pair formation in magnesium electrolytes from first-principles quantum mechanics and classical molecular dynamics. *J. Am. Chem. Soc.* 137: 3411–3420.

51 Law, Y.T., Schnaidt, J., Brimaud, S., and Behm, R.J. (2016). Oxygen reduction and evolution in an ionic liquid ([BMP][TFSA]) based electrolyte: a model study of the cathode reactions in Mg–air batteries. *J. Power Sources* 333: 173–183.

52 Watkins, T. and Buttry, D.A. (2015). Determination of Mg^{2+} speciation in a $TFSI^-$-based ionic liquid with and without chelating ethers using Raman spectroscopy. *J. Phys. Chem. B* 119: 7003–7014.

53 Mohtadi, R., Matsui, M., Arthur, T.S., and Hwang, S.-J. (2012). Magnesium borohydride from hydrogen storage to magnesium battery. *Angew. Chem. Int. Ed.* 51: 9780–9783.

54 Watkins, T., Kumar, A., and Buttry, D.A. (2016). Designer ionic liquids for reversible electrochemical deposition/dissolution of magnesium. *J. Am. Chem. Soc.* 138: 641–650.

55 Tutusaus, O., Mohtadi, R., Arthur, T.S. et al. (2015). An efficient halogen-free electrolyte for use in rechargeable magnesium batteries. *Angew. Chem. Int. Ed.* 54: 7900–7904.

56 Carter, T.J., Mohtadi, R., Arthur, T.S. et al. (2014). Boron clusters as highly stable magnesium-battery electrolytes. *Angew. Chem. Int. Ed.* 53 (12): 3173–3177.

57 Vardar, G., Nelson, E.G., Smith, J.G. et al. (2015). Identifying the discharge product and reaction pathway for a secondary Mg/O_2 battery. *Chem. Mater.* 27: 7564–7568.

58 Leskes, M., Moore, A.J., Goward, G.R., and Grey, C.P. (2013). Monitoring the electrochemical processes in the lithium–air battery by solid state NMR spectroscopy. *J. Phys. Chem. C* 117: 26929–26939.

59 Laoire, C.O., Mukerjee, S., Abraham, K.M. et al. (2009). Elucidating the mechanism of oxygen reduction for lithium–air battery applications. *J. Phys. Chem. C* 113: 20127–20134.

60 Peng, Z., Freunberger, S.A., Chen, Y., and Bruce, P.G. (2012). A reversible and higher-rate Li–O_2 battery. *Science* 337: 563–566.

61 Bender, C.L., Hartmann, P., Vračar, M. et al. (2014). On the thermodynamics, the role of the carbon cathode, and the cycle life of the sodium superoxide (NaO_2) Battery. *Adv. Energy Mater.* 4: 1301863.

62 Hartmann, P., Bender, C.L., Sann, J. et al. (2013). A comprehensive study on the cell chemistry of the sodium superoxide (NaO_2) battery. *Phys. Chem. Chem. Phys.* 15: 11661–11672.

63 Torres, W., Mozhzhukhina, N., Tesio, A.Y., and Calvo, E.J. (2014). A rotating ring disk electrode study of the oxygen reduction reaction in lithium containing dimethyl sulfoxide electrolyte: role of superoxide. *J. Electrochem. Soc.* 161: A2204–A2209.

64 Griffith, L.D., Sleightholme, A.E.S., Mansfield, J.F. et al. (2015). Correlating Li/O_2 cell capacity and product morphology with discharge current. *Appl. Mater. Interfaces* 7: 7670–7678.

65 Nazar, L., Adams, B., Black, R. et al. (2013). Current density dependence of peroxide formation in the Li–O_2 battery and its effect on charge. *Energy Environ. Sci.* .

66 Yadegari, H., Li, Y., Banis, M.N. et al. (2014). On rechargeability and reaction kinetics of sodium–air batteries. *Energy Environ. Sci.* 7: 3747–3757.

67 Nelson, E.G., Brody, S.I., Kampf, J.W., and Bartlett, B.M. (2014). A magnesium tetraphenylaluminate battery electrolyte exhibits a wide electrochemical potential window and reduces stainless steel corrosion. *J. Mater. Chem. A* 2: 18194–18198.

68 Ren, X., Lau, K.C., Yu, M. et al. (2014). Understanding side reactions in K–O_2 batteries for improved cycle life. *ACS Appl. Mater. Interfaces* 6: 19299–19307.

69 Girishkumar, G., McCloskey, B., Luntz, A.C. et al. (2010). Lithium—air battery: promise and challenges. *J. Phys. Chem. Lett.* 1: 2193–2203.

70 Shiga, T., Hase, Y., Kato, Y. et al. (2013). A rechargeable non-aqueous Mg–O_2 battery. *Chem. Commun.* 49: 9152–9154.

71 Yagi, S., Tanaka, a., Ichitsubo, T., and Matsubara, E. (2012). Electrochemical stability of metal electrodes for reversible magnesium deposition/dissolution in tetrahydrofuran dissolving ethylmagnesium chloride. *ECS Electrochem. Lett.* 1: D11–D14.

72 Guo, Y., Yang, J., NuLi, Y., and Wang, J. (2010). Study of electronic effect of Grignard reagents on their electrochemical behavior. *Electrochem. Commun.* 12: 1671–1673.

73 Cooper, C. (2010). *Organic Chemist's Desk Reference*. Chapman and Hall/CRC.

74 Barile, C.J., Nuzzo, R.G., and Gewirth, A.A. (2015). Exploring salt and solvent effects in chloride-based electrolytes for magnesium electrodeposition and dissolution. *J. Phys. Chem. C* 119: 13524–13534.

75 Canepa, P., Jayaraman, S., Cheng, L. et al. (2015). Elucidating the structure of the magnesium aluminum chloride complex electrolyte for magnesium-ion batteries. *Energy Environ. Sci.* 8: 3718–3730.

76 Pan, B., Huang, J., Sa, N. et al. (2016). $MgCl_2$: the key ingredient to improve chloride containing electrolytes for rechargeable magnesium-ion batteries. *J. Electrochem. Soc.* 163: A1672–A1677.

77 Sa, N., Pan, B., Saha-Shah, A. et al. (2016). Role of chloride for a simple, non-Grignard Mg electrolyte in ether based solvents. *ACS Appl. Mater. Interfaces* doi: 10.1021/acsami.6b03193.

78 Zhao-Karger, Z., Zhao, X., Fuhr, O., and Fichtner, M. (2013). Bisamide based non-nucleophilic electrolytes for rechargeable magnesium batteries. *RSC Adv.* 3: 16330.

79 Zhao-Karger, Z., Mueller, J.E., Zhao, X. et al. (2014). Novel transmetalation reaction for electrolyte synthesis for rechargeable magnesium batteries. *RSC Adv.* 4: 26924–26927.

80 Liao, C., Sa, N., Key, B. et al. (2015). The unexpected discovery of the $Mg(HMDS)_2/MgCl_2$ complex as a magnesium electrolyte for rechargeable magnesium batteries. *J. Mater. Chem. A* 3: 6082–6087.

81 Shterenberg, I., Salama, M., Yoo, H.D. et al. (2015). Evaluation of $(CF_3SO_2)_2N^-$ (TFSI) based electrolyte solutions for Mg batteries. *J. Electrochem. Soc.* 162: A7118–A7128.

82 Muldoon, J., Bucur, C.B., Oliver, A.G. et al. (2013). Corrosion of magnesium electrolytes: chlorides – the culprit. *Energy Environ. Sci.* 6: 482.

83 Shiga, T., Hase, Y., Yagi, Y. et al. (2014). Catalytic cycle employing a TEMPO – anion complex to obtain a secondary Mg–O_2 battery. *J. Phys. Chem. Lett.* 5: 1648–1652.

84 Liu, J., Rahimian, S.K., and Monroe, C.W. (2016). Capacity-limiting mechanisms in Li/O_2 batteries. *Phys. Chem. Chem. Phys.* .

85 Lu, Y.-C., Kwabi, D.G., Yao, K.P.C. et al. (2011). The discharge rate capability of rechargeable Li–O_2 batteries. *Energy Environ. Sci.* 4: 2999–3007.

86 Quaranta, M., Murkovic, M., and Klimant, I. (2013). A new method to measure oxygen solubility in organic solvents through optical oxygen sensing. *Analyst* 138: 6243–6245.

87 Johnson, L., Li, C., Liu, Z. et al. (2014). The role of LiO_2 solubility in O_2 reduction in aprotic solvents and its consequences for Li–O_2 batteries. *Nat. Chem.* 6: 1091–1099.

88 Stern, K.H. (1974). High temperature properties and decomposition of inorganic salts. Part 4: Oxy-salts of the halogens. *J. Phys. Chem. Ref. Data* 3: 481.

89 Kumar, N., Radin, M.D., Wood, B.C. et al. (2015). Surface-mediated solvent decomposition in Li–air batteries: impact of peroxide and superoxide surface terminations. *J. Phys. Chem. C* 119: 9050–9060.

90 Doerffel, D. and Sharkh, S.A. (2006). A critical review of using the Peukert equation for determining the remaining capacity of lead-acid and lithium–ion batteries. *J. Power Sources* 155: 395–400.

91 Baert, D. and Vervaet, A. (1999). Lead-acid battery model for the derivation of Peukert's law. *Electrochim. Acta* 44: 3491–3504.

92 Viswanathan, V., Norskov, J.K., Speidel, A. et al. (2013). Li–O_2 kinetic overpotentials: Tafel plots from experiment and first-principles theory. *J. Phys. Chem. Lett.* 4: 556–560.

93 Tutusaus, O., Mohtadi, R., Singh, N. et al. (2017). Study of electrochemical phenomena observed at the Mg metal/electrolyte interface. *ACS Energy Lett.* 2: 224–229.

94 Schwenke, K.U., Meini, S., Wu, X. et al. (2013). Stability of superoxide radicals in glyme solvents for non-aqueous Li–O_2 battery electrolytes. *Phys. Chem. Chem. Phys.* 15: 11830–11839.

95 Zhang, T. and Zhou, H. (2013). A reversible long-life lithium–air battery in ambient air. *Nat. Commun.* 4: 1817.

96 Irvine, J.T.S., Sinclair, D.C., and West, A.R. (1990). Electroceramics: characterization by impedance spectroscopy. *Adv. Mater.* 2: 132–138.

97 Smith, J.G., Naruse, J., Hiramatsu, H., and Siegel, D.J. (2016). Theoretical limiting potentials in Mg/O_2 batteries. *Chem. Mater.* 28: 1390–1401.

98 Smith, J.G., Naruse, J., Hiramatsu, H., and Siegel, D.J. (2017). Intrinsic conductivity in magnesium–oxygen battery discharge products: MgO and MgO_2. *Chem. Mater.* 29: 3152–3163.

99 Dong, Q., Yao, X., Luo, J. et al. (2016). Enabling rechargeable non-aqueous Mg–O_2 battery operations with dual redox mediators. *Chem. Commun.* 52: 13753–13756.

100 Radin, M.D., Rodriguez, J.F., Tian, F., and Siegel, D.J. (2012). Lithium peroxide surfaces are metallic, while lithium oxide surfaces are not. *J. Am. Chem. Soc.* 134: 1093–1103.

101 Chase, M.W. (1998). *NIST-JANAF Thermochemical Tables*, 4e. American Institute of Physics.

102 Coughlin, J. (1954). *Bulletin 542 Contributions to the Data of Theoretical Metallurgy*. Washington, D.C.: Bureau of Mines.

103 Volnov, I.I., Tokareva, S.A., Belevskii, V.N., and Latysheva, E.I. (1970). The formation of magnesium perperoxide in the reaction of magnesium peroxide with ozone. *Izv. Akad. Nauk SSSR* 3: 468–471.

104 Vannerberg, N. (1959). The formation and structure of magnesium peroxide. *Ark. foer. Kemi* 14: 99–105.

105 Volnov, I. and Latysheva, E. (1970). Thermal stability of magnesium peroxide. *Izv. Akad. Nauk SSSR* 1: 13–18.

106 Bakulina, V.M., Tokareva, S.A., Latysheva, E.I., and Vol'nov, I.I. (1970). X-ray diffraction study of magnesium superoxide $Mg(O_2)_2$. *J. Struct. Chem.* 11: 150–151.

107 Kresse, G. and Hafner, J. (1993). Ab initio molecular dynamics for liquid metals. *Phys. Rev. B* 47: 558–561.

108 Kresse, G. and Hafner, J. (1994). Ab initio molecular-dynamics simulation of the liquid-metal–amorphous-semiconductor transition in germanium. *Phys. Rev. B* 49: 14251–14269.

109 Kresse, G. and Furthmuller, J. (1996). Efficiency of ab-initio total energy calculations for metals and semiconductors using a plane-wave basis set. *Comput. Mater. Sci.* 6: 15–50.

110 Kresse, G. and Furthmüller, J. (1996). Efficient iterative schemes for ab initio total-energy calculations using a plane-wave basis set. *Phys. Rev. B: Condens. Matter* 54: 11169–11186.

111 Nørskov, J.K., Rossmeisl, J., Logadottir, A. et al. (2004). Origin of the overpotential for oxygen reduction at a fuel-cell cathode. *J. Phys. Chem. B* 108: 17886–17892.

112 Hummelshøj, J.S., Luntz, A.C., and Nørskov, J.K. (2013). Theoretical evidence for low kinetic overpotentials in Li–O_2 electrochemistry. *J. Chem. Phys.* 138: 034703–034712.

113 Chen, L.D., Norskov, J.K., and Luntz, A.C. (2015). Al–air batteries: fundamental thermodynamic limitations from first-principles theory. *J. Phys. Chem. Lett.* 6: 175–179.

114 Radin, M.D., Tian, F., and Siegel, D.J. (2012). Electronic structure of Li_2O_2 {0001} surfaces. *J. Mater. Sci.* 47: 7564–7570.

115 Radin, M.D. and Siegel, D.J. (2013). Charge transport in lithium peroxide: relevance for rechargeable metal–air batteries. *Energy Environ. Sci.* 6: 2370–2379.

116 Tian, F., Radin, M.D., and Siegel, D.J. (2014). Enhanced charge transport in amorphous Li_2O_2. *Chem. Mater.* 26: 2952–2959.

117 Radin, M.D., Monroe, C.W., and Siegel, D.J. (2015). Impact of space-charge layers on sudden death in Li/O_2 batteries. *J. Phys. Chem. Lett.* 6: 3017–3022.

118 Radin, M.D., Monroe, C.W., and Siegel, D.J. (2015). How dopants can enhance charge transport in Li_2O_2. *Chem. Mater.* 27: 839–847.

119 Heyd, J., Scuseria, G.E., and Ernzerhof, M. (2003). Hybrid functionals based on a screened Coulomb potential. *J. Chem. Phys.* 118: 8207–8215.

120 Krukau, A.V., Vydrov, O.A., Izmaylov, A.F., and Scuseria, G.E. (2006). Influence of the exchange screening parameter on the performance of screened hybrid functionals. *J. Chem. Phys.* 125: 224106.

121 Shishkin, M. and Kresse, G. (2006). Implementation and performance of the frequency-dependent GW method within the PAW framework. *Phys. Rev. B* 74: 35101.

122 Shishkin, M., Marsman, M., and Kresse, G. (2007). Accurate quasiparticle spectra from self-consistent GW calculations with vertex corrections. *Phys. Rev. Lett.* 99: 246403.

123 Mackrodt, W.C. (1982). Defect calculations for ionic materials. In: *Computer Simulation of Solids* (ed. W.C. Mackrodt and C.R.A. Catlow), 175. Berlin: Springer-Verlag.

124 Henkelman, G., Uberuaga, B.P., and Jónsson, H. (2000). A climbing image nudged elastic band method for finding saddle points and minimum energy paths. *J. Chem. Phys.* 113: 9901–9904.

125 Henkelman, G. and Jónsson, H. (2000). Improved tangent estimate in the nudged elastic band method for finding minimum energy paths and saddle points. *J. Chem. Phys.* 113: 9978–9985.

126 Garcia-Lastra, J.M., Myrdal, J.S.G., Christensen, R. et al. (2013). DFT+U study of polaronic conduction in Li_2O_2 and Li_2CO_3: implications for Li–air batteries. *J. Phys. Chem. C* 117: 5568–5577.

127 Yang, S. and Siegel, D.J. (2015). Intrinsic conductivity in sodium–air battery discharge phases: sodium superoxide vs sodium peroxide. *Chem. Mater.* 27: 3852–3860.

128 Sasaki, K. and Maier, J. (1999). Low-temperature defect chemistry of oxides. I. General aspects and numerical calculations. *J. Appl. Phys.* (10): 5422–5433.
129 Kroger, F.A. and Vink, H.J. (1956). Relations between the concentrations of imperfections in crystalline solids. *Solid State Phys.* 3: 307–435.
130 Kroger, F.A. (1964). *The Chemistry of Imperfect Crystals*. Amsterdam: North-Holland Publishing Company.
131 Lidiard, A. (1957). *Handbuch Der Physik*, vol. XX (ed. S. Flugge). Berlin: Springer-Verlag.
132 Maier, J. (2003). Complex oxides: high temperature defect chemistry vs. low temperature defect chemistry. *Phys. Chem. Chem. Phys.* 5: 2164–2173.
133 Maier, J. (2004). High temperature versus low temperature defect chemistry. *Solid State Ionics* 173: 1–8.
134 Kathrein, H. and Freund, F. (1983). Electrical conductivity of magnesium oxide single crystal below 1200 K. *J. Phys. Chem. Solids* 44: 177–186.
135 Freund, F., Freund, M., and Batllo, F. (1993). Critical review of electrical conductivity measurements and charge distribution analysis of magnesium oxide. *J. Geophys. Res.* 98: 209–229.
136 Kathrein, H., Knipping, U., and Freund, F. (1980). Atomic carbon in magnesium oxide. Part VI: Electrical conductivity. *Mat. Res. Bull.* 15: 1393–1399.
137 Mitoff, S.P. (1959). Electrical conductivity of single crystals of MgO. *J. Chem. Phys.* 31: 1261–1269.
138 Lempicki, A. (1953). The electrical conductivity of MgO single crystals at high temperatures. *Proc. Phys. Soc.* 66: 281–283.
139 Batllo, F., Leroy, R.C., Parvin, K., and Freund, F. (1990). Dissociation of O_2^{-2} defects into paramagnetic O^- in wide band-gap insulators: a magnetic susceptibility study of magnesium oxide. *J. Appl. Phys.* 67: 5844–5846.